Comparison of the Capability of Remote Sensing Data to Characterize the Feature of Interest: Three Case Studies

Rosa Maria Cavalli

CNR-IRPI, via della Madonna Alta 126, Perugia

e-mail: rosa.maria.cavalli@irpi.cnr.it

1. Study of **suspended particulate matter (SPM)** in coastal and inland waters
2. Characterization and mapping of **impervious urban surface materials**
3. Detection the “**discontinuity**” in the soil and first subsoil (e.g., soil displacements and surface deformations, buried archaeological structures) that can produce “mark” on the images

Suspended particulate matter (SPM)

Sentinel 2, band 3 [560nm], Cervaro stream mouth (FG), 2018/01/03

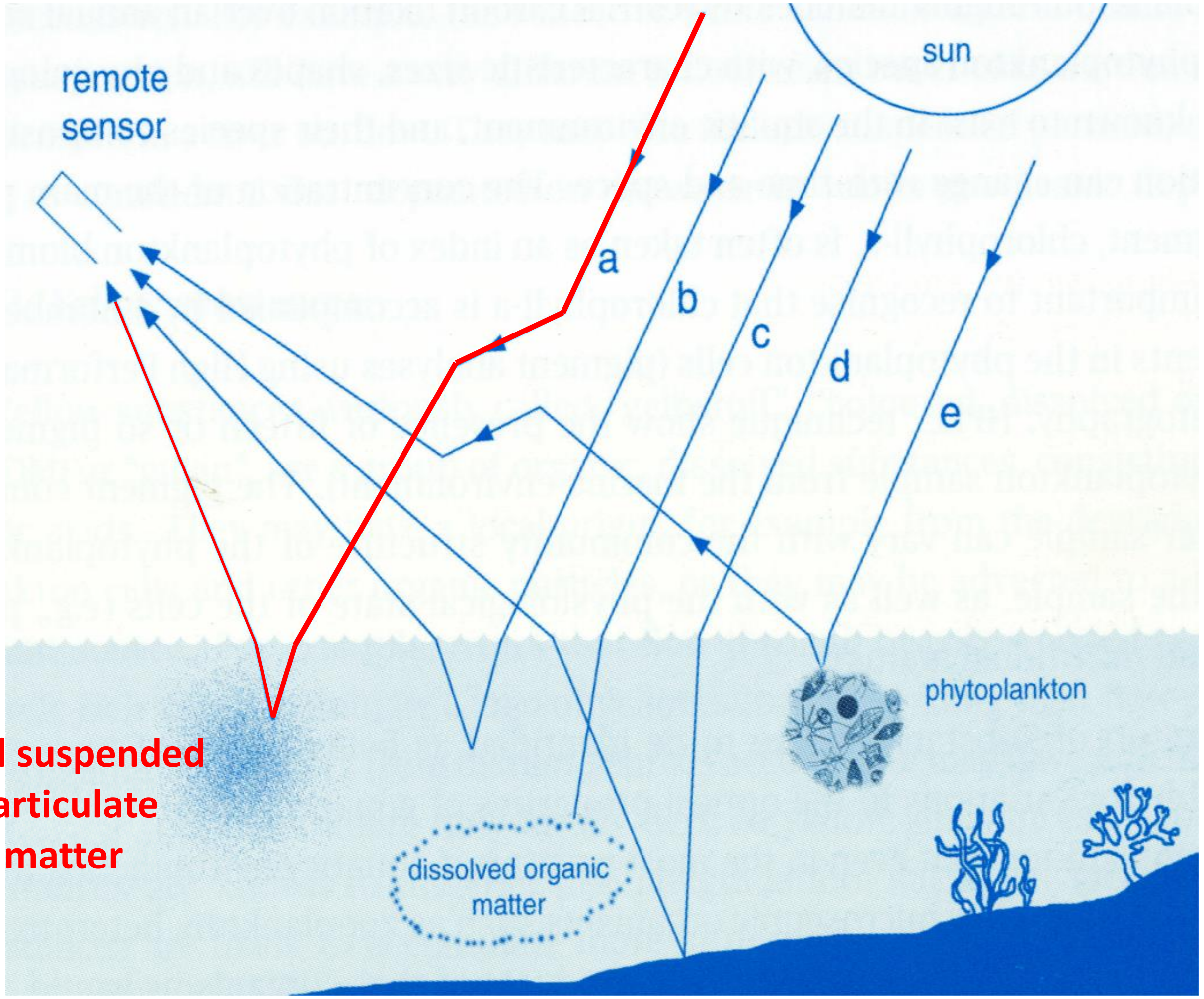

Suspended particulate matter (SPM)

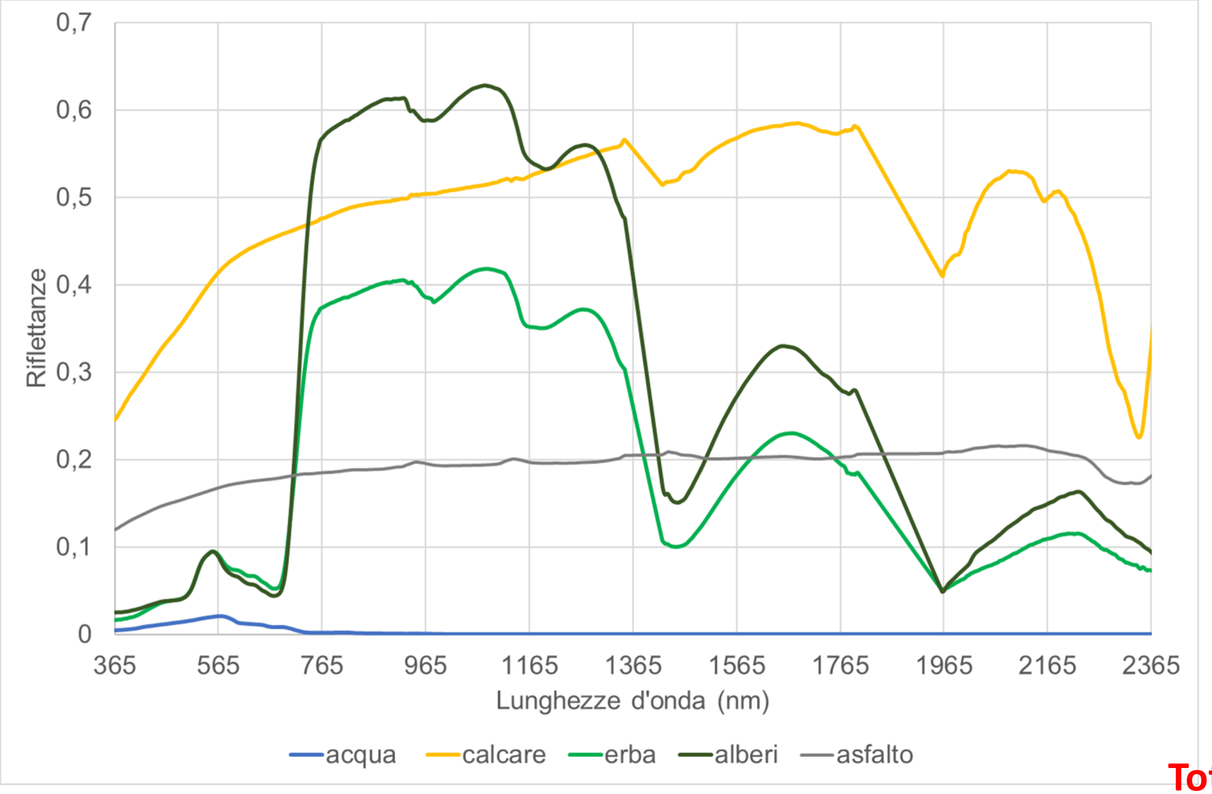

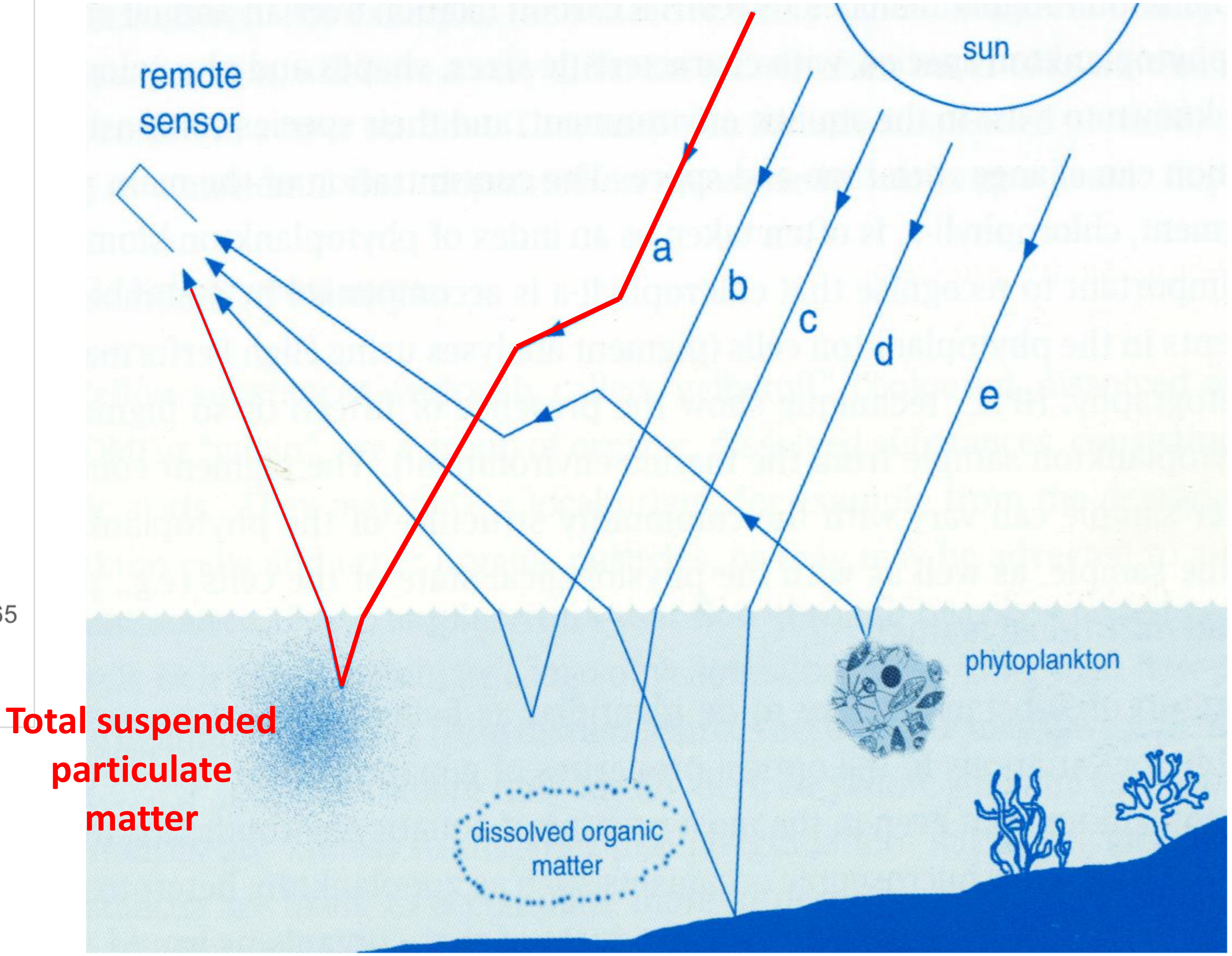

Suspended particulate matter (SPM)

The literature classifies bio-optical algorithms into two macro classes (Ogaskawara, 2015):

Empirical models exploit statistical relationships between AOPs and water constituent concentrations measured in situ

e.g. $[TSM] = \alpha(R_1/R_2)^{\beta} + \gamma.$

Analytical models utilize radiative transfer theory

$$\mu \frac{dL\left(z,\hat{\xi},\lambda\right)}{dz} = -c\left(z,\lambda\right) L\left(z,\hat{\xi},\lambda\right) + \\ + \oint L\left(z,\hat{\xi}',\lambda\right) \beta\left(z,\hat{\xi}' \rightarrow \hat{\xi},\lambda\right) d\Omega\left(\hat{\xi}'\right) + S\left(z,\hat{\xi},\lambda\right)$$

Suspended particulate matter (SPM)

Manfredonia Gulf

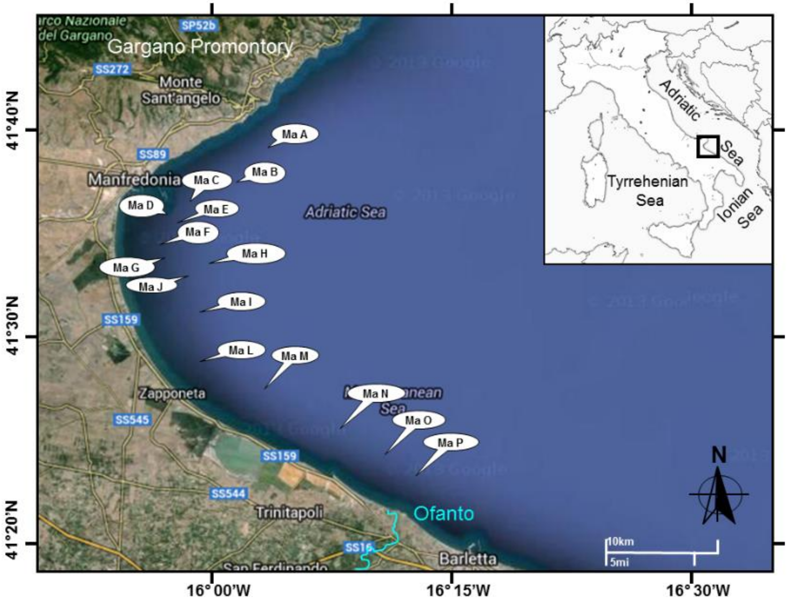

Sampling of these locations were carried out during four days, and principal locations were monitored several times:

in total, **36 water columns** were characterized (Cavalli et al., 2014).

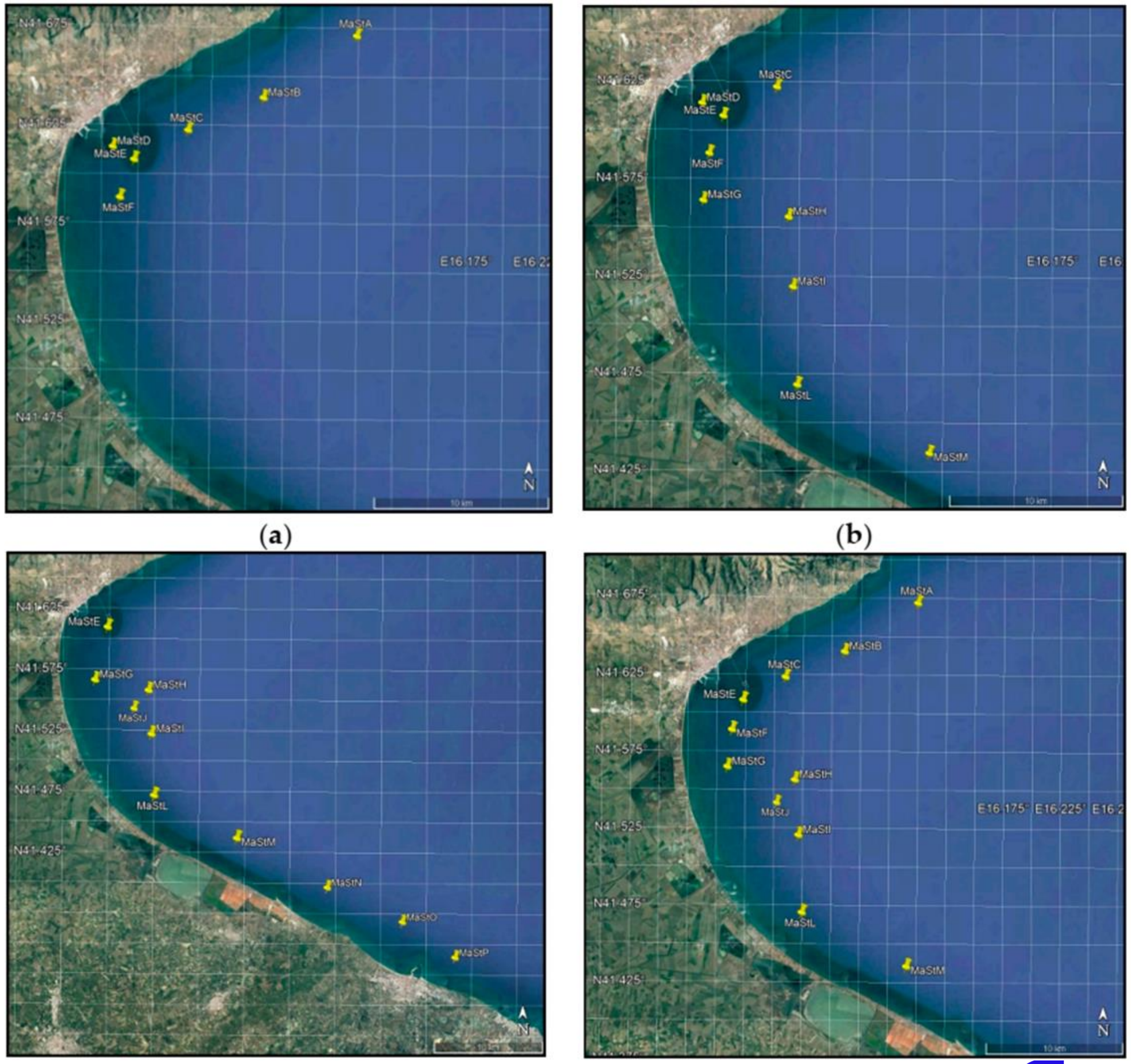

41 simplified analitical models

Cavalli, 2020

Suspended particulate matter (SPM)

Manfredonia Gulf

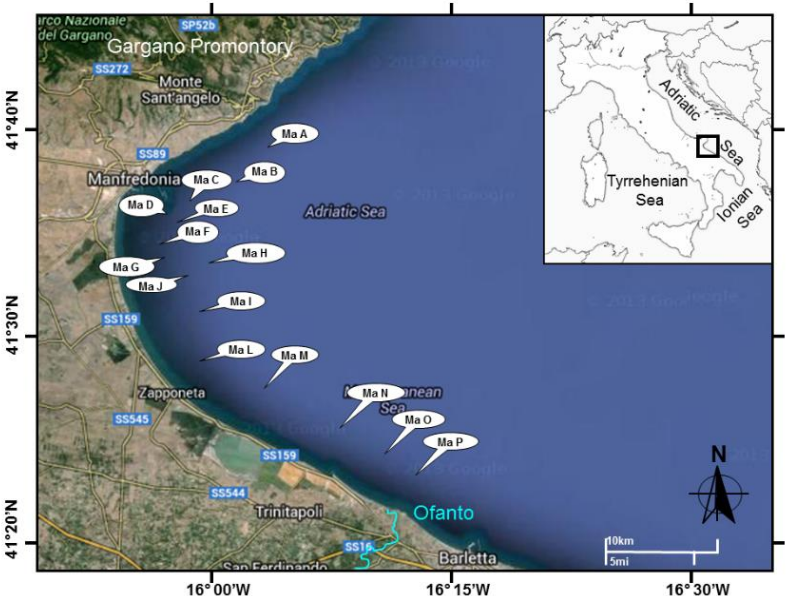

Sampling of these locations were carried out during four days, and principal locations were monitored several times:
in total, **36 water columns** were characterized (Cavalli et al., 2014).

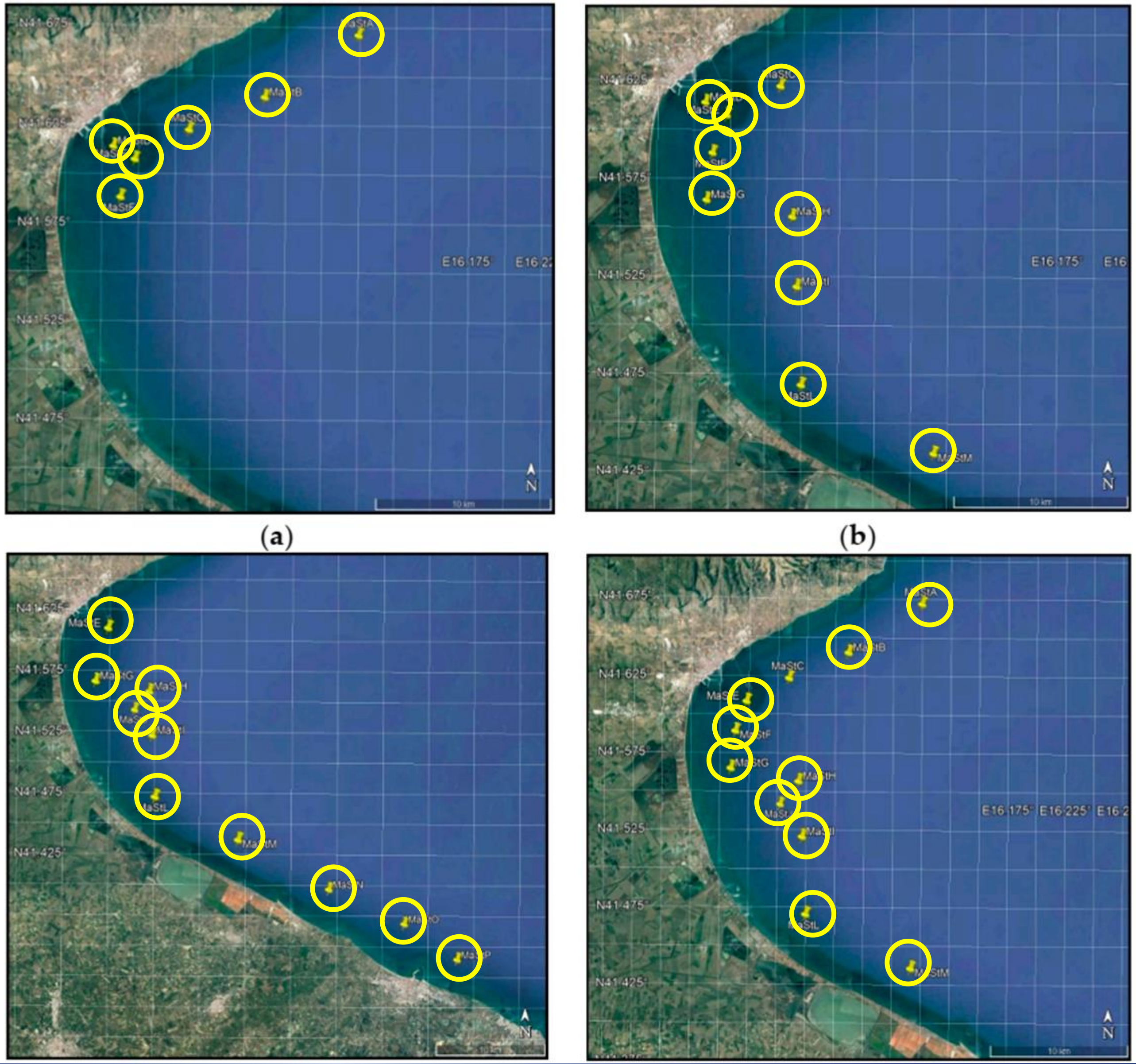

36 local models

Cavalli, 2020

Suspended particulate matter (SPM)

Manfredonia Gulf

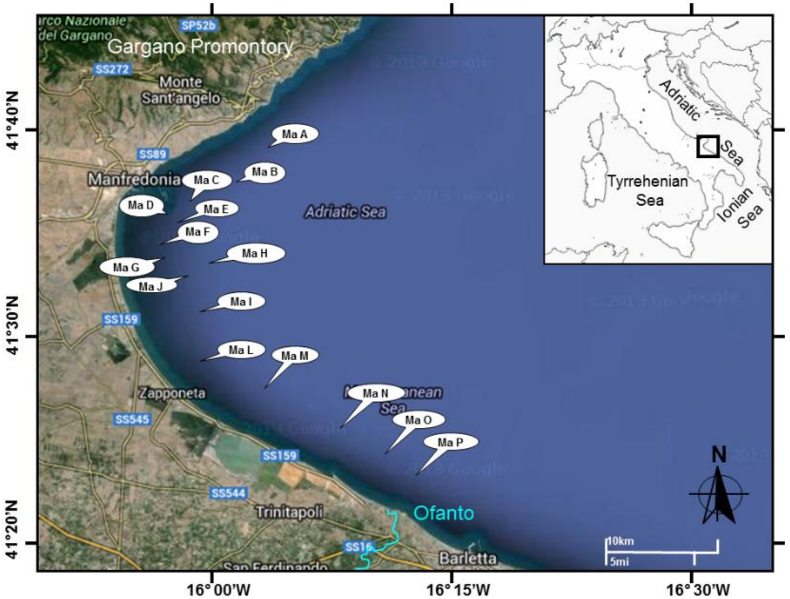

Sampling of these locations were carried out during four days, and principal locations were monitored several times:
in total, **36 water columns** were characterized (Cavalli et al., 2014).

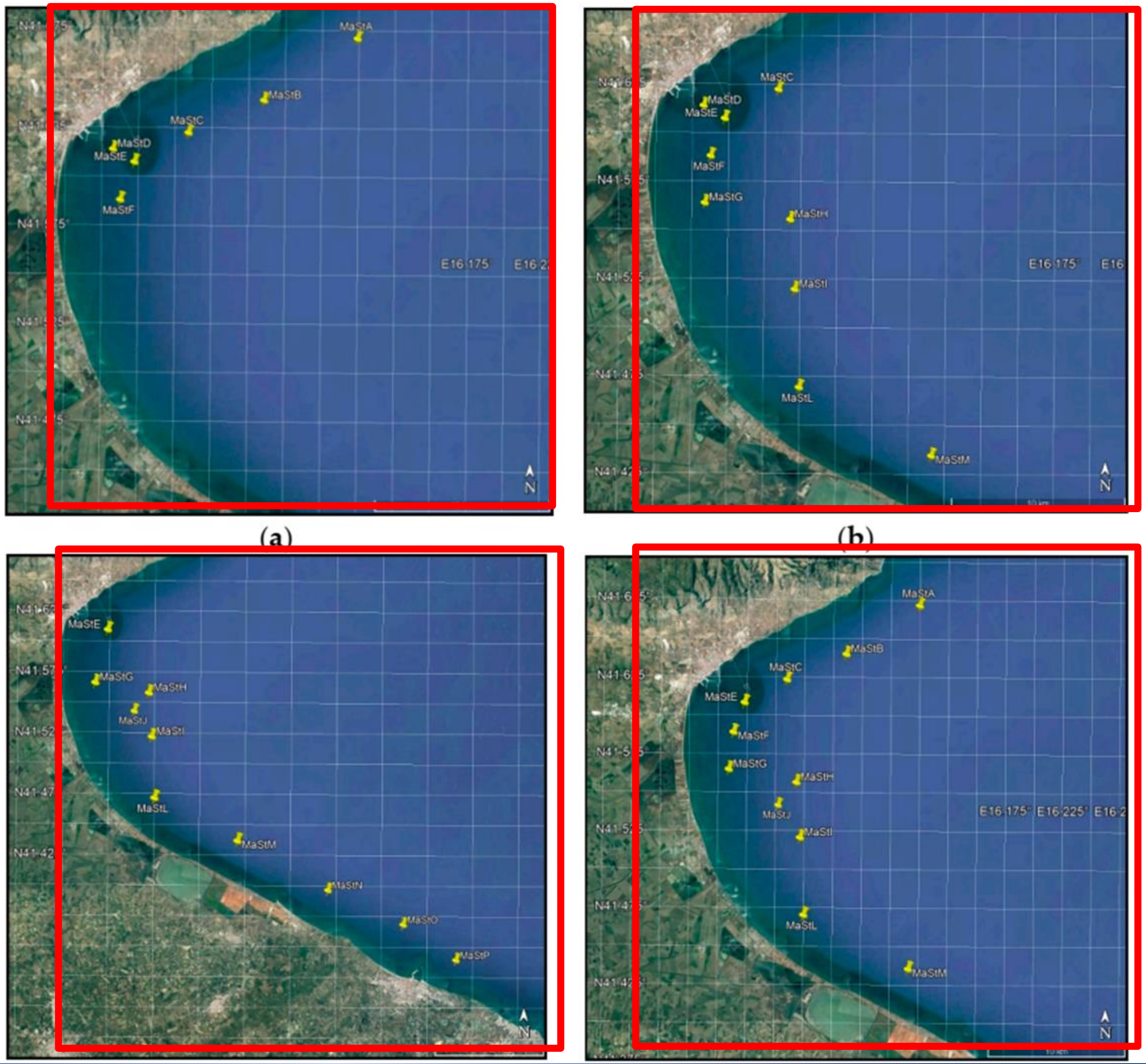

4 daily models

Cavalli, 2020

Suspended particulate matter (SPM)

Manfredonia Gulf

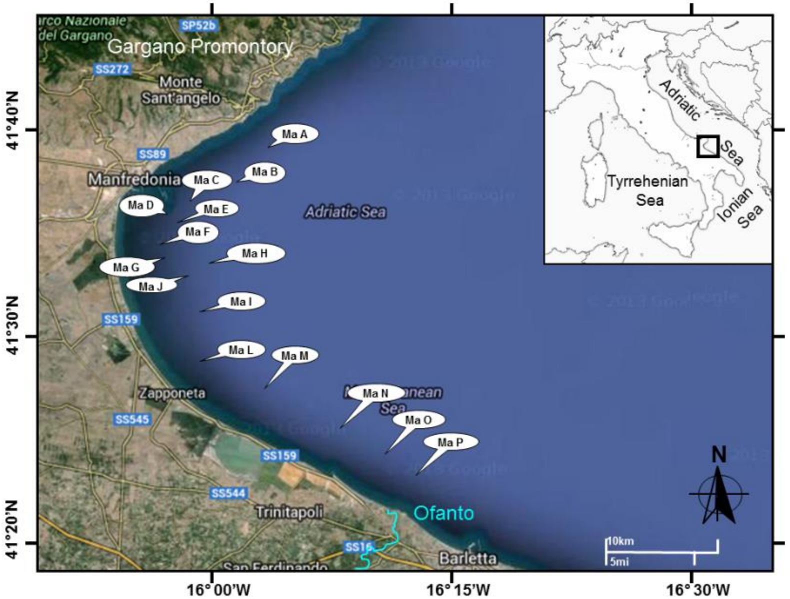

Sampling of these locations were carried out during four days, and principal locations were monitored several times:
in total, **36 water columns** were characterized (Cavalli et al., 2014).

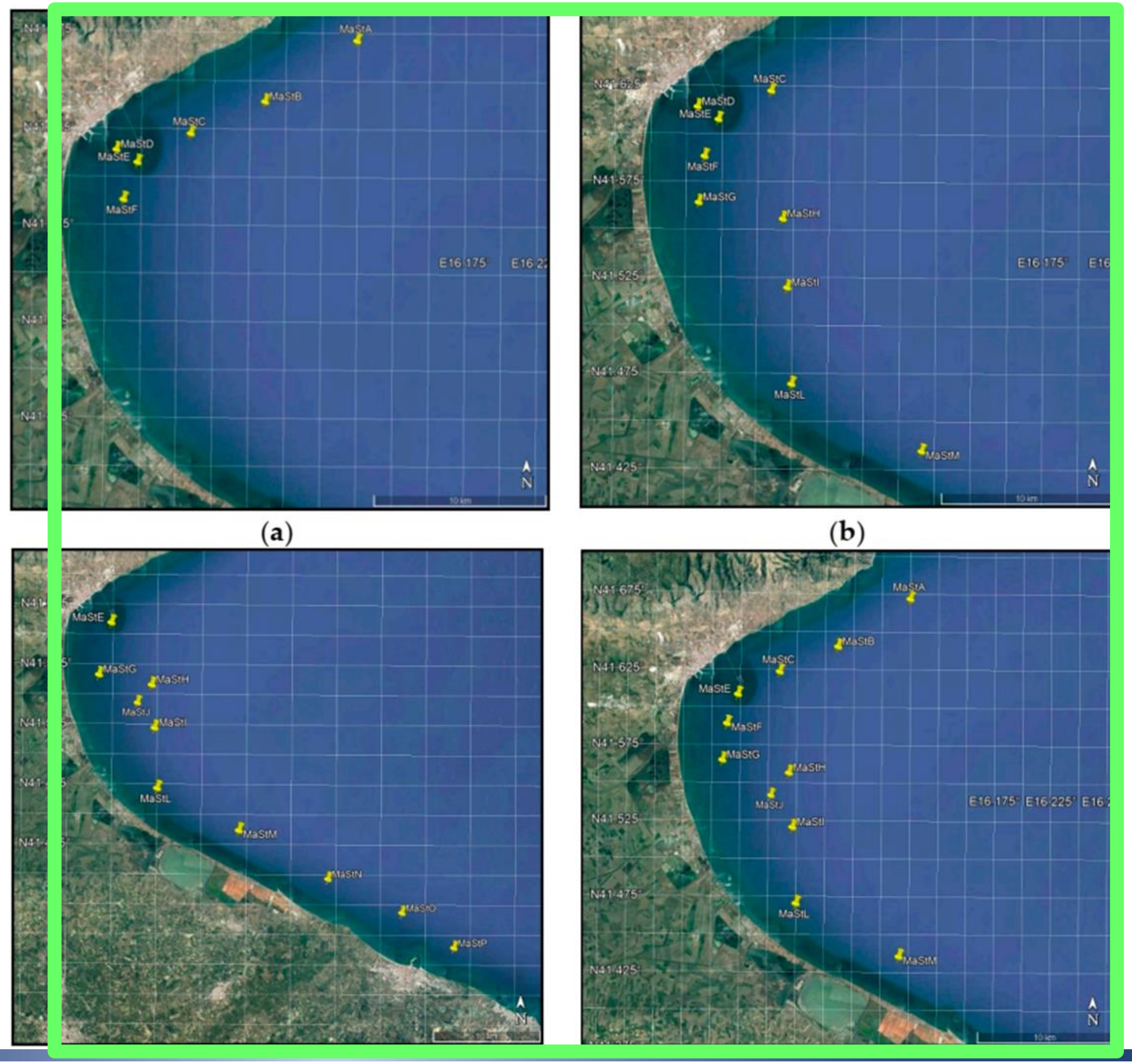

1 total model

Cavalli, 2020

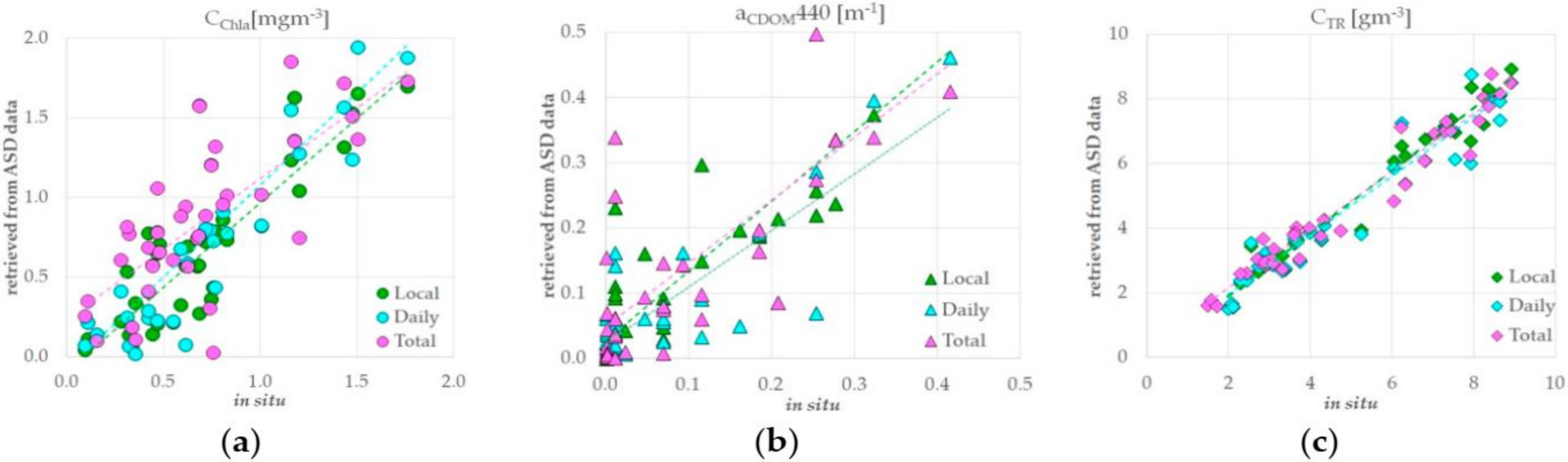

Figure 3. Scatter plots of retrieved products using local, daily, and total bio-optical models and in situ concentrations: (**a**) retrieved concentrations of chlorophyll-a vs. in situ data; (**b**) retrieved a_{CDOM} at 440 nm vs. in situ data; (**c**) retrieved concentrations of tripton vs. in situ data.

Bio−Optical Models		Slope	Intercept	R^2	$mean_{bias}$	σ_{bias}	bias %	KGE
C_{Chla} (mgm^{-3})	Local	1.06	−0.09	0.83	0.05	0.20	10%	0.80
	Daily	1.16	−0.08	0.77	−0.03	0.27	12%	0.65
	Total	0.88	0.23	0.56	−0.15	0.32	17%	0.62
a_{CDOM} 440 (m^{-1})	Local	1.07	0.03	0.77	−0.03	0.07	11%	0.54
	Daily	0.87	0.02	0.70	−0.01	0.06	11%	0.78
	Total	0.97	0.05	0.54	−0.05	0.10	15%	0.31
C_{TR} (gm^{-3})	Local	0.97	0.03	0.97	0.12	0.35	3%	0.96
	Daily	0.87	0.23	0.92	0.23	0.52	5%	0.92
	Total	0.85	0.51	0.94	0.14	0.54	6%	0.91

Cavalli, 2020

Errors in C_{Chla} calculated from some sensors using **local bio-optical models**

sensor	slope	interc.	R^2	bias	dev	bias %	KGE
ASD	1.06	-0.09	0.83	0.05	0.20	10%	0.80
PRISMA	1.00	0.08	0.52	-0.08	0.39	15%	0.51
CHRIS mode 1	0.80	0.08	0.48	0.05	0.43	15%	0.51
CHRIS mode 2	0.80	0.08	0.43	0.05	0.43	15%	0.51
MIVIS	0.78	0.36	0.43	-0.21	0.38	22%	0.51
MODIS	1.00	0.09	0.46	-0.09	0.44	22%	0.42
Landsat TM				-0.19	2.45	112%	-3.89

Errors in C_{CDOM} calculated from some sensors using **local bio-optical models**

sensor	slope	interc.	R^2	bias	dev	bias %	KGE
ASD	1.07	0.03	0.77	-0.03	0.07	11%	0.54
PRISMA	0.81	0.07	0.59	-0.05	0.08	15%	0.35
MIVIS	1.06	0.05	0.42	-0.02	0.11	16%	0.46
CHRIS mode 1	0.96	0.02	0.43	-0.02	0.12	19%	0.40
CHRIS mode 2	0.78	0.06	0.41	-0.04	0.12	19%	0.44
MODIS	0.73	0.09	0.35	-0.07	0.11	21%	0.03
Landsat TM				0.36	2.66	386%	-22.71

Errors in C_{TR} calculated from some sensors using **total bio-optical model**

sensor	slope	interc.	R^2	bias	dev	bias %	KGE
ASD	0.85	0.51	0.94	0.14	0.54	6%	0.91
MIVIS	0.79	0.78	0.88	0.35	0.76	8%	0.83
CHRIS mode 1	0.72	0.68	0.90	0.59	0.85	10%	0.75
CHRIS mode 2	0.71	1.37	0.85	0.07	0.99	10%	0.75
PRISMA	0.72	0.81	0.89	0.57	0.89	11%	0.73
MODIS	0.69	0.68	0.67	0.87	1.38	14%	0.70
Landsat TM	0.62	1.53	0.46	0.34	1.84	20%	0.66

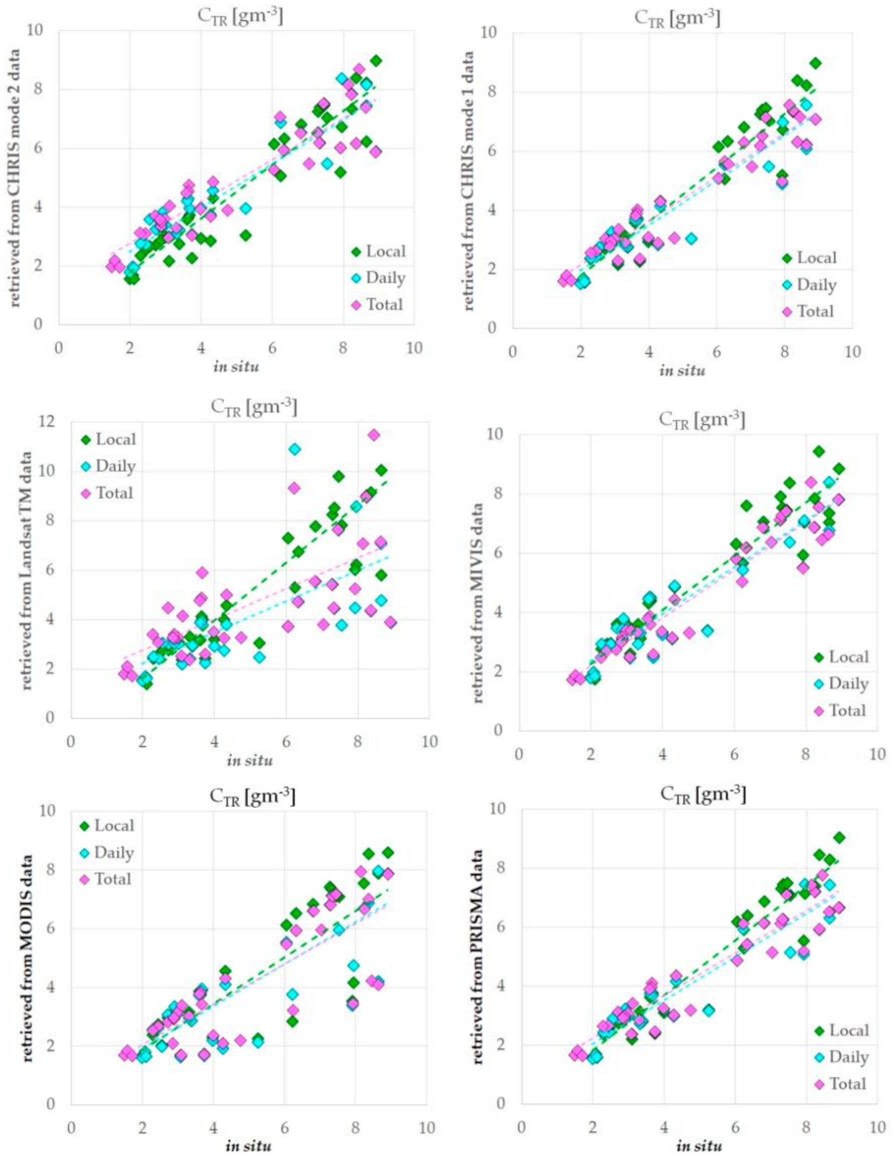

Suspended particulate matter (SPM) and Sea Surface Emissivity (SSE)

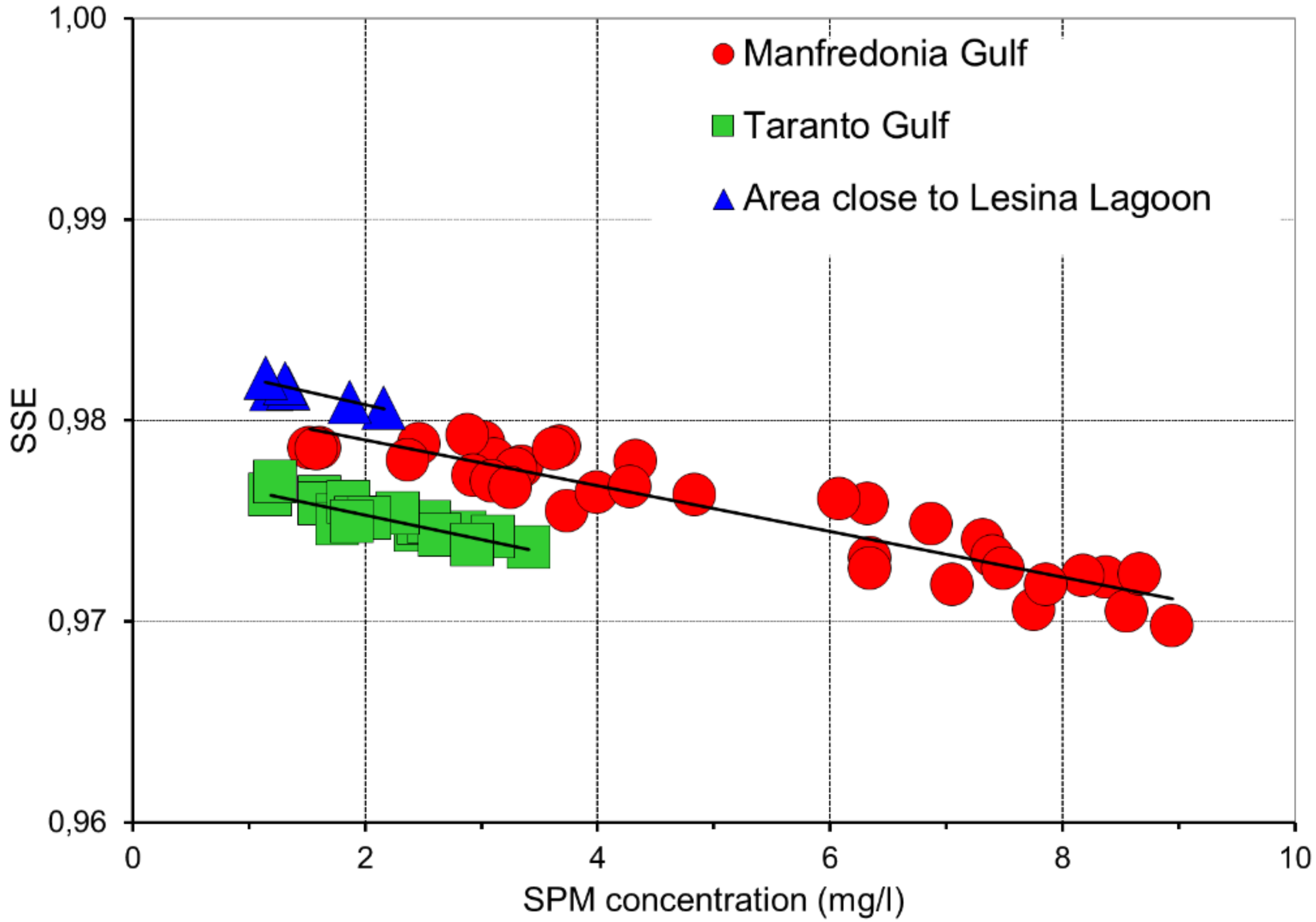

Cavalli, 2017

Figure 5. SSE behavior with respect to SPM concentration in these coastal waters.

RMSD (K) between SST_{skin} data and SST measurements obtained from MODIS data

Coastal waters of	MODIS Aqua Global Level 3 Mapped Thermal SST data (K)	SST data (K) retrieved by [35]		
		with SSE (SPM=0)	with SSE (SPM≠0) using Wen-Yao at al. [46]	with SSE (SPM≠0) using Equations (7)-(9)
the Manfredonia Gulf	1.22	0.95	0.92	0.72
the Taranto Gulf	1.12	0.76	0.76	0.64
area close to Lesina Lagoon	1.49	0.66	0.66	0.60

SST_{skin} data compared with SST measurements	which were retrieved using the algorithm proposed by	RMSD (K)	Max Bias (K)	Mean σ (K)
LST2	Sobrino *et al.* [37]	0.48	-3.45	0.41
SST3	Sobrino *et al.* [37]	0.58	-3.48	0.42
LST1	Wan and Dozier [38]	0.66	-1.37	0.35
SST4	Sobrino *et al.* [37]	0.67	-3.82	0.39
SST2 (collezione 6)	Kilpatrick *et al.* [17]	0.68	-1.90	0.40
SST1 (Collezione 5)	Kilpatrick *et al.* [18]	0.76	-2.29	0.41
LST3	Sobrino *et al.* [37]	0.77	-4.97	0.40
SST6	Niclos *et al.* [41]	0.84	-3.13	0.47
SST1 (ECMWF based)	Brown *et al.* [16]	1.14	-3.77	0.45
SST1 (radiosonde based)	Brown *et al.* [16]	2.41	-5.53	0.46
SST5	Sobrino *et al.* [37]	2.45	-5.41	0.42
LST4	Sobrino *et al.* [37]	3.56	5.79	0.45

SSE $= f$ (SPM)

SSE not required as explicit input

Cavalli, 2017
Cavalli, 2018

References

- Cavalli, R. M., Laneve, G., Fusilli, L., Pignatti, S., & Santini, F. (2009). Remote sensing water observation for supporting Lake Victoria weed management. Journal of environmental management, 90(7), 2199-2211.
- Cavalli, R. M., Betti, M., Campanelli, A., Cicco, A. D., Guglietta, D., Penna, P., & Piermattei, V. (2014). A methodology to assess the accuracy with which remote data characterize a specific surface, as a Function of Full Width at Half Maximum (FWHM): Application to three Italian coastal waters. *Sensors*, *14*(1), 1155-1183.
- Cavalli, R. M. (2017). Retrieval of sea surface temperature from MODIS data in coastal waters. *Sustainability*, *9*(11), 2032.
- Cavalli, R. M. (2018). Comparison of split window algorithms for retrieving measurements of sea surface temperature from MODIS data in near-land coastal waters. *ISPRS International Journal of Geo-Information*, *7*(1), 30.
- Cavalli, R. M. (2020). Local, daily, and total bio-optical models of coastal waters of manfredonia gulf applied to simulated data of CHRIS, Landsat TM, MIVIS, MODIS, and PRISMA Sensors for Evaluating the Error. *Remote Sensing*, *12*(9), 1428.
- 35. Niclòs, R.; Caselles, V.; Coll, C.; Valor, E. Determination of sea surface temperature at large observation angles using an angular and emissivity-dependent split-window equation. Remote Sens. Environ. 2007, 111, 107–121. [CrossRef]
- Ogashawara, I.; Mishra, D.R.; Gitelson, A.A. Remote sensing of inland waters: Background and current state-of-the-art. In Bio-Optical Modeling and Remote Sensing of Inland Waters; Mishra, D.R., Ogashawara, I., Gitelson, A.A., Eds.; Elsevier: Amsterdam, The Netherlands, 2017; pp. 1–24.

- Santini, F., Alberotanza, L., Cavalli, R. M., & Pignatti, S. (2010). A two-step optimization procedure for assessing water constituent concentrations by hyperspectral remote sensing techniques: An application to the highly turbid Venice lagoon waters. Remote Sensing of Environment, 114(4), 887-898.
- 16. Brown, O.B.; Minnett, P.J.; Evans, R.; Kearns, E.; Kilpatrick, K.; Kumar, A.; Sikorski, R.; Závody, A. MODIS Infrared Sea Surface Temperature Algorithm Algorithm Theoretical Basis Document, Version 2.0; University of Miami: Miami, FL, USA, 1999; pp. 1–91.
- 17. Kilpatrick, K.; Podesta, G.;Walsh, S.; Evans, R.; Minnett, P. Implementation of Version 6 AQUA and TERRA SST Processing; White Paper; University of Miami: Coral Gables, FL, USA, 2014.
- 18. Kilpatrick, K.A.; Podestá, G.; Walsh, S.; Williams, E.; Halliwell, V.; Szczodrak, M.; Brown, O.B.; Minnett, P.J.; Evans, R. A decade of sea surface temperature from MODIS. Remote Sens. Environ. 2015, 165, 27–41.[CrossRef]
- 37. Sobrino, J.A.; El Kharraz, J.; Li, Z.L. Surface temperature and water vapour retrieval from MODIS data. Int. J. Remote Sens. 2003, 24, 5161–5182. [CrossRef]
- 38. Wan, Z.M.; Dozier, J. A generalized split-window algorithm for retrieving land surface temperature from space. IEEE Trans. Geosci. Remote Sens. 1996, 34, 892–905.
- 41. Niclòs, R.; Caselles, V.; Coll, C.; Valor, E. Determination of sea surface temperature at large observation angles using an angular and emissivity-dependent split-window equation. Remote Sens. Environ. 2007, 111, 107–121. [CrossRef]
- 46. Wen-Yao, L.; Field, R.T.; Gantt, R.G.; Klemas, V. Measurement of the surface emissivity of turbid waters. Remote Sens. Environ. **1987**, 21, 97–109. [CrossRef]

Impervious urban surface materials

Data Spatial Resolution	Sensors: Panchromatic	Sensors: Multispectral	Sensors: Hyperspectral	Optical Spectral Bands	Optical Spectral Cover (nm)	References
Urban cover mapping at urban scale						
High (<10 m)	IRS-1C			1	500–750	[29] [1]
	IKONOS			1	530–930	[17] [1]; [26] [1]; [29] [1]; [31] [1,2]
	QuickBird			1	405–1053	[35] [1,2]
	WorldView-2			1	450–800	[28] [1,2]; [30] [1,2]
		IKONOS		4	450–860	[17] [1]; [26] [1]; [29] [1]
		QuickBird		5	403–918	[27] [1,2]; [35] [1,2]
		WorldView-2		8	400–1040	[28] [1,2]; [30] [1,2]
			APEX	288	372–2540	[18] [1]
			AVIRIS	244	365–2500	[19] [1]
			DAIS	72	400–2500	[20] [1,2]
			HyMap	128	400–2500	[21] [1,2]
			MIVIS	92	430–2478	[31] [1,2]; [22] [1,2]
Moderate (10 m–100 m)	SPOT			1	450–750	[34] [1,2]; [35] [1,2]
		ALI		9	433–2350	[31] [1,2]
		Landsat TM		6	450–2350	[32] [1,2]; [34] [1,2]; [36] [1,2]
		Landsat ETM+		6	450–2350	[31] [1,2]; [32] [1,2]; [35] [1,2]; [36] [1,2]; [37] [1,2]; [38] [1,2]
		Sentinel 2a		12	443–2200	[33] [1,2]
		SPOT		4	450–890	[34] [1,2]
			CHRIS	19–150	410–1050	[23] [1,2]
			Hyperion	242	400–2500	[24] [1,2]; [25] [1]; [31] [1,2]
			TG-1	128	400–2500	[25] [1]
Urban cover mapping at country and global scale						
Coarse (>100 m)		DMSP-OLS		2	400–1100	[39] [1,2];
		MERIS		15	390–1040	[37] [1,2]
		MODIS		19	405–2155	[36] [1,2]; [40] [1,2]; [41] [1,2]

[1] The study merged multi-source data. [2] The study combined different techniques.

Small, 2003

Tran et al., 2011

Cavalli et al., 2008

Cavalli, 2021

Impervious urban surface materials

Hyperspectral Library

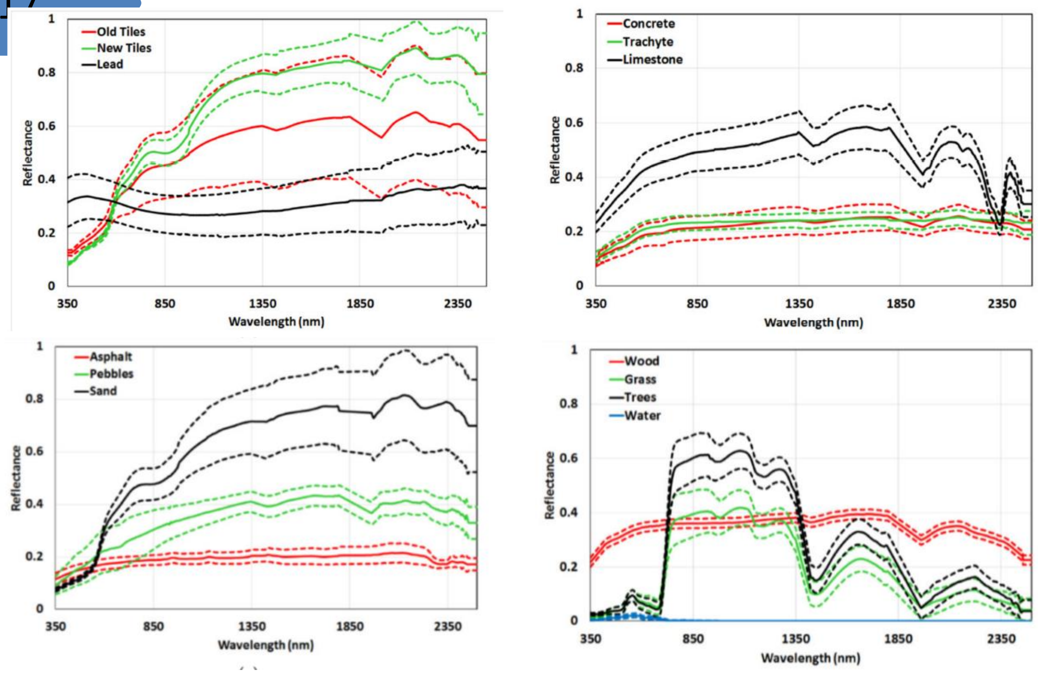

Abrams et al., 2003

Santini et al., 2010

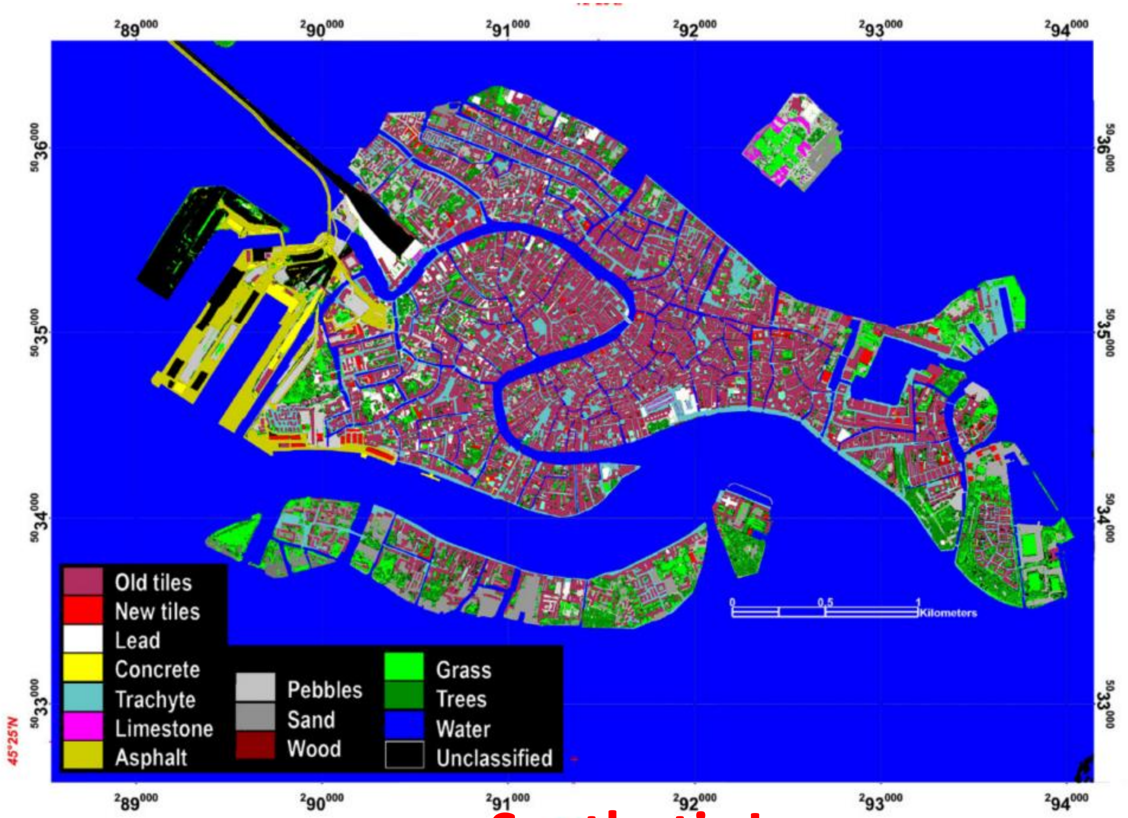

Synthetic Image

Table 3. Spectral ranges, spectral resolutions, which were represented with Full Width at Half Maximum (FWHM), and spatial resolutions of most remote sensing sensors.

Spectral Cover Range (nm)	FWHM (nm)	Spatial Resolution (m)
365–2500	3; 10; 30; 50; 100	1; 5; 10; 50; 100; 250
400–1100	3; 10; 30; 50; 100	1; 5; 10; 50; 100; 250

Cavalli, 2021

Values obtained from images with spectral range of 365–2500 nm

Imperviuos surfaces

KGE — Spatial resolution (m) × Spectral resolution (nm)

Spectral resolution (nm)	1	5	10	50	100	250
3	0.49	0.56	0.59	0.05	0.14	0.02
10	0.45	0.57	0.57	-0.37	0.11	0.01
30	0.47	0.55	0.56	0.02	0.10	-0.15
50	0.38	0.46	0.55	0.02	0.08	-0.15
100	0.24	0.39	0.54	0.01	0.08	-0.26

mean standard deviation = 0.16

Total Errors

Spectral resolution (nm)	1	5	10	50	100	250
3	13%	16%	17%	37%	39%	38%
10	15%	16%	18%	39%	38%	38%
30	13%	15%	17%	37%	39%	39%
50	16%	18%	18%	37%	39%	40%
100	18%	18%	17%	37%	39%	43%

mean standard deviation = 6%

Perviuos surfaces

KGE — Spatial resolution (m) × Spectral resolution (nm)

Spectral resolution (nm)	1	5	10	50	100	250
3	0.43	0.50	0.24	-0.29	-4.02	-2.70
10	0.43	0.49	0.24	-0.49	-4.11	-3.19
30	0.43	0.49	0.25	-0.44	-4.13	-3.18
50	0.40	0.49	0.24	-0.42	-4.11	-3.16
100	0.34	0.47	0.25	-0.34	-4.12	-3.07

mean standard deviation = 0.99

Total Errors

Spectral resolution (nm)	1	5	10	50	100	250
3	19%	35%	44%	54%	54%	54%
10	27%	35%	43%	55%	54%	53%
30	19%	30%	40%	54%	54%	53%
50	25%	34%	43%	54%	54%	52%
100	23%	29%	39%	53%	53%	51%

mean standard deviation = 12%

Values obtained from images with spectral range of 400–1100 nm

Imperviuos surfaces

KGE — Spatial resolution (m) × Spectral resolution (nm)

Spectral resolution (nm)	1	5	10	50	100	250
3	0.21	0.30	0.51	0.00	-0.40	-0.03
10	0.20	0.29	0.49	-0.02	-0.78	0.01
30	0.20	0.26	0.42	-0.41	-0.54	-0.32
50	0.19	0.16	0.25	-0.51	-0.79	-0.82
100	-0.15	-0.02	0.22	-0.38	-0.16	-0.33

mean standard deviation = 0.59

Total Errors

Spectral resolution (nm)	1	5	10	50	100	250
3	25%	25%	19%	35%	40%	34%
10	26%	25%	20%	35%	40%	34%
30	31%	29%	23%	36%	40%	33%
50	34%	30%	24%	36%	39%	32%
100	59%	57%	53%	21%	24%	27%

mean standard deviation = 6%

Perviuos surfaces

KGE — Spatial resolution (m) × Spectral resolution (nm)

Spectral resolution (nm)	1	5	10	50	100	250
3	0.31	0.43	0.16	-0.18	-30.95	-2.61
10	0.35	0.50	0.18	-0.19	-30.95	-2.87
30	0.33	0.48	0.20	-0.19	-30.95	-2.91
50	0.32	0.39	0.06	-0.19	-30.96	-3.09
100	0.15	0.31	0.06	-0.17	-38.82	-2.71

mean standard deviation = 1.29

Total Errors

Spectral resolution (nm)	1	5	10	50	100	250
3	32%	39%	49%	61%	59%	63%
10	28%	33%	49%	60%	58%	62%
30	27%	33%	48%	59%	56%	61%
50	28%	31%	45%	58%	51%	57%
100	58%	58%	63%	67%	58%	67%

mean standard deviation = 12%

Cavalli, 2021

References

17. Small, C. High spatial resolution spectral mixture analysis of urban reflectance. Remote Sens. Environ. 2003, 88, 170–186. [CrossRef]
18. Priem, F.; Canters, F. Synergistic Use of LiDAR and APEX Hyperspectral Data for High-Resolution Urban Land Cover Mapping. Remote Sens. 2016, 8, 787. [CrossRef]
19. Alonzo, M.; Bookhagen, B.; Roberts, D.A. Urban tree species mapping using hyperspectral and lidar data fusion. Remote Sens.Environ. 2014, 148, 70–83. [CrossRef]
20. Segl, K.; Roessner, S.; Heiden, U.; Kaufmann, H. Fusion of spectral and shape features for identification of urban surface cover types using reflective and thermal hyperspectral data. ISPRS J. Photogramm. Remote Sens. 2003, 58, 99–112. [CrossRef]
21. Heiden, U.; Roessner, S.; Segl, K.; Kaufmann, H. Analysis of spectral signatures of urban surfaces for their identification using hyperspectral HyMap data. In Proceedings of the IEEE/ISPRS JointWorkshop on Remote Sensing and Data Fusion over Urban
Areas (Cat. No.01EX482), Rome, Italy, 8–9 November 2001; pp. 173–177. [CrossRef]
22. Forzieri, G.; Tanteri, L.; Moser, G.; Catani, F. Mapping natural and urban environments using airborne multi-sensor ADS40–MIVIS–LiDAR synergies. Int. J. Appl. Earth Obs. Geoinf. 2013, 23, 313–323. [CrossRef]
23. Demarchi, L.; Canters, F.; Chan, J.C.W.; Van de Voorde, T. Multiple endmember unmixing of CHRIS/Proba imagery for mapping impervious surfaces in urban and suburban environments. IEEE Trans. Geosci. Remote Sens. 2012, 50, 3409–3424. [CrossRef]
24. Zhang, C. Multiscale quantification of urban composition from EO-1/Hyperion data using object-based spectral unmixing. Int. J.Appl. Earth Obs. Geoinf. 2016, 47, 153–162. [CrossRef]
25. Li, X.;Wu, T.; Liu, K.; Li, Y.; Zhang, L. Evaluation of the Chinese Fine Spatial Resolution Hyperspectral Satellite TianGong-1 in Urban Land-Cover Classification. Remote Sens. 2016, 8, 438. [CrossRef]

26. Herold, M.; Goldstein, N.C.; Clarke, K.C. The spatiotemporal form of urban growth: Measurement, analysis and modeling. Remote Sens. Environ. 2003, 86, 286–302. [CrossRef]
27. Tooke, T.R.; Coops, N.C.; Goodwin, N.R.; Voogt, J.A. Extracting urban vegetation characteristics using spectral mixture analysis and decision tree classifications. Remote Sens. Environ. 2009, 113, 398–407. [CrossRef] [CrossRef]
28. Longbotham, N.; Chaapel, C.; Bleiler, L.; Padwick, C.; Emery, W.J.; Pacifici, F. Very high resolution multiangle urban classification analysis. IEEE Trans. Geosci. Remote Sens. 2011, 50, 1155–1170. [CrossRef]
29. Benediktsson, J.A.; Pesaresi, M.; Amason, K. Classification and feature extraction for remote sensing images from urban areas based on morphological transformations. IEEE Trans. Geosci. Remote Sens. 2003, 41, 1940–1949. [CrossRef]
30. Xu, R.; Zhang, H.;Wang, T.; Lin, H. Using pan-sharpened high resolution satellite data to improve impervious surfaces estimation. Int. J. Appl. Earth Obs. Geoinf. 2017, 57, 177–189. [CrossRef]
31. Cavalli, R.M.; Fusilli, L.; Pascucci, S.; Pignatti, S.; Santini, F. Hyperspectral sensor data capability for retrieving complex urban land cover in comparison with multispectral data: Venice city case study (Italy). Sensors 2008, 8, 3299–3320. [CrossRef]
32. Song, X.P.; Sexton, J.O.; Huang, C.; Channan, S.; Townshend, J.R. Characterizing the magnitude, timing and duration of urban growth from time series of Landsat-based estimates of impervious cover. Remote Sens. Environ. 2016, 175, 1–13. [CrossRef]
33. Luo, X.; Tong, X.; Hu, Z.;Wu, G. Improving Urban Land Cover/use Mapping by Integrating A Hybrid Convolutional Neural Network and An Automatic Training Sample Expanding Strategy. Remote Sens. 2020, 12, 2292. [CrossRef]
34. Banzhaf, E.; Grescho, V.; Kindler, A. Monitoring urban to peri-urban development with integrated remote sensing and GIS information: A Leipzig, Germany case study. Int. J. Remote Sens. 2009, 30, 1675–1696. [CrossRef]
35. Tran, T.D.B.; Puissant, A.; Badariotti, D.; Weber, C. Optimizing spatial resolution of imagery for urban form detection—the cases of France and Vietnam. Remote Sens. 2011, 3, 2128–2147. [CrossRef]

36. Schneider, A.; Friedl, M.A.; Potere, D. Mapping global urban areas using MODIS 500-m data: New methods and datasets based on 'urban ecoregions'. Remote Sens. Environ. 2010, 114, 1733–1746. [CrossRef]
37. Arino, O.; Gross, D.; Ranera, F.; Leroy, M.; Bicheron, P.; Brockman, C.; Bourg, L. GlobCover: ESA service for global land cover from MERIS. In Proceedings of the 2007 IEEE International Geoscience and Remote Sensing Symposium, Barcelona, Spain, 23–28 July 2007; pp. 2412–2415.
38. Lu, D.; Weng, Q. Use of impervious surface in urban land-use classification. Remote Sens. Environ. 2006, 102, 146–160. [CrossRef]
39. Shao, Z.; Liu, C. The integrated use of DMSP-OLS nighttime light and MODIS data for monitoring large-scale impervious surface dynamics: A case study in the Yangtze River Delta. Remote Sens. 2014, 6, 9359–9378. [CrossRef] Remote Sens. 2021, 13, 3959 29 of 29
40. Mertes, C.M.; Schneider, A.; Sulla-Menashe, D.; Tatem, A.J.; Tan, B. Detecting change in urban areas at continental scales with MODIS data. Remote Sens. Environ. 2015, 158, 331–347. [CrossRef]
41. Deng, C.;Wu, C. The use of single-date MODIS imagery for estimating large-scale urban impervious surface fraction with spectral mixture analysis and machine learning techniques. ISPRS J. Photogramm. Remote Sens. 2013, 86, 100–110. [CrossRef]
Santini, F.; Alberotanza, L.; Cavalli, R.M.; Pignatti, S. A two-step optimization procedure for assessing water constituent concentrations by hyperspectral remote sensing techniques: An application to the highly turbid Venice lagoon waters. Remote Sens. Environ. **2010**, 114, 887–898. [CrossRef]
Abrams, M.; Cavalli, R.M.; Pignatti, S. Intercalibration and fusion of satellite and airborne multispectral data over Venice. In Proceedings of the 2nd GRSS/ISPRS JointWorkshop on Remote Sensing and Data Fusion over Urban Areas, Berlin, Germany, 22–23 May 2003.
Cavalli, R. M. (2021). Capability of Remote Sensing Images to Distinguish the Urban Surface Materials: A Case Study of Venice City. *Remote Sensing*, *13*(19), 3959.

Detection of “marks”

Selinunte

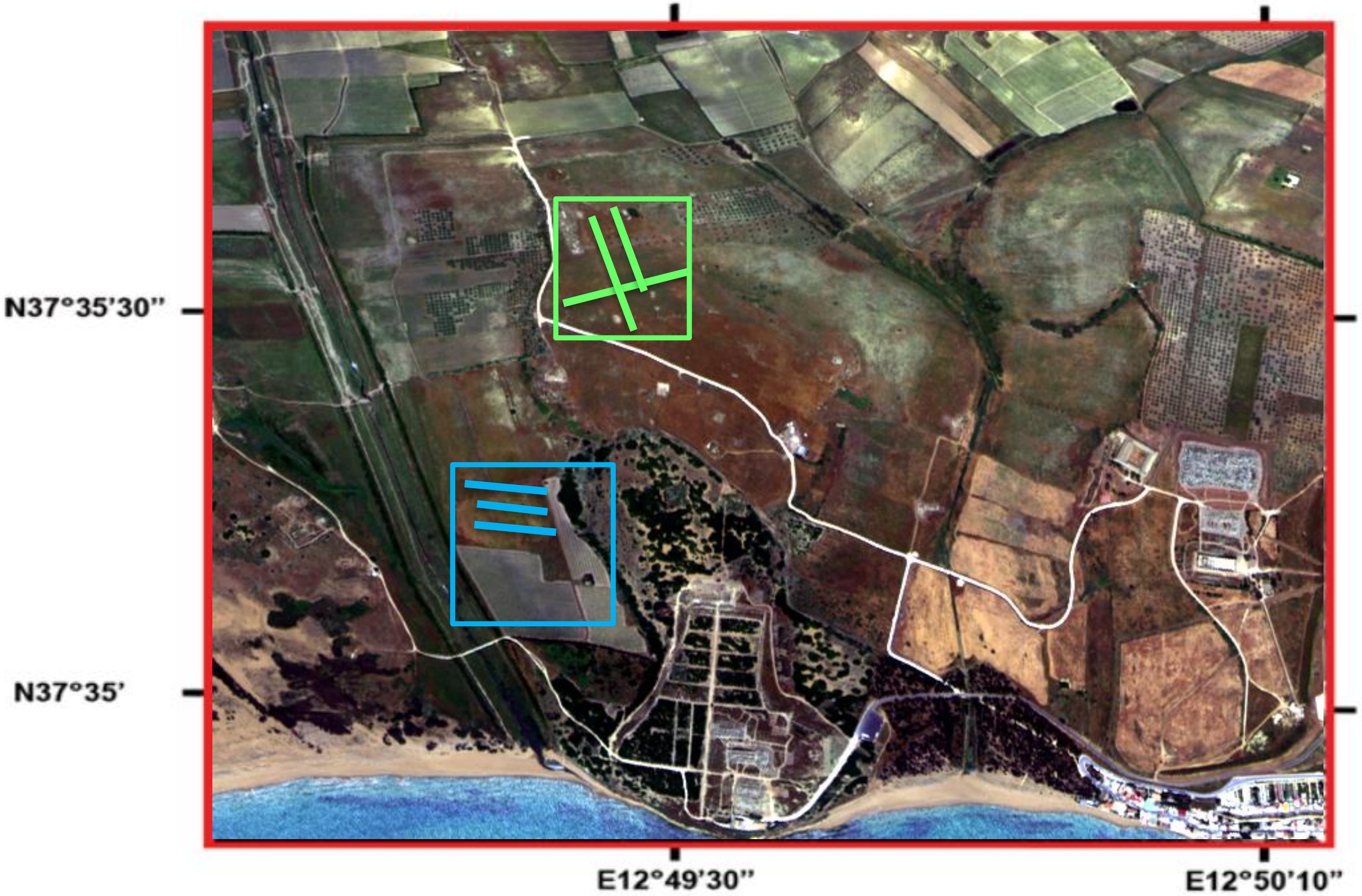

Cavalli et al., 2007, 2013

Cerra et al., 2018

Detection of “marks”

Rank C	Rank S	Index	Equation	Ref.
26	31	Anthocyanin Reflectance Index 1	$ARI1 = \frac{1}{\rho_{550}} - \frac{1}{\rho_{700}}$	[44]
35	30	Anthocyanin Reflectance Index 2	$ARI2 = \rho_{800}[\frac{1}{\rho_{550}} - \frac{1}{\rho_{700}}]$	[44]
12	8	Atmospherically Resistant Vegetation Index	$ARVI = \frac{NIR - [Red - \gamma(Blue - Red)]}{NIR + [Red - \gamma(Blue - Red)]}$	[30]
1	34	Burned Area Index	$BAI = \frac{1}{(0.1 - Red)^2 + (0.06 - NIR)^2}$	[32,45]
25	21	Carotenoid Reflectance Index 1	$CRI1 = \frac{1}{\rho_{510}} - \frac{1}{\rho_{550}}$	[46]
28	29	Carotenoid Reflectance Index 2	$CRI2 = \frac{1}{\rho_{510}} - \frac{1}{\rho_{700}}$	[46]
18	20	Difference Vegetation Index	$DVI = NIR - Red$	[47]
22	9	Enhanced Vegetation Index	$EVI = 2.5\frac{NIR - Red}{NIR + 6 * Red - 7.5 * Blue + 1}$	[48]
11	19	Global Environmental Monitoring Index	$GEMI = 0.75\,\eta - \frac{Red - 0.125}{1 - Red}$, where $\eta = \frac{2(NIR^2 - Red^2) + 1.5NIR + 0.5Red}{NIR + Red + 0.5}$	[38]
17	14	Green Atmospherically Resistant Index	$GARI = \frac{NIR - [Green - \gamma(Blue - Red)]}{NIR - [Green - \gamma(Blue + Red)]}$	[49]
16	32	Green Difference Vegetation Index	$GDVI = NIR - Green$	[50]
14	24	Green NDVI	$GNDVI = \frac{GDVI}{NIR + Green}$	[51]
5	26	Green Ratio Vegetation Index	$GRVI = \frac{NIR}{Green}$	[50]
9	15	Infrared Percentage Vegetation Index	$IPVI = \frac{NIR}{NIR + Red}$	[52]

Rank C	Rank S	Index	Equation	Ref.
30	23	Iron Oxide	$IronOxide = \frac{Red}{Blue}$	[53]
31	3	Modified CARI	$MCARI = (0.8\,\rho_{700} - \rho_{670} + 0.2\,\rho_{550})\frac{\rho_{700}}{\rho_{670}}$	[54]
19	6	Modified CARI—Improved	$MCARI2 = \frac{1.5[2.5(\rho_{800} - \rho_{670}) - 1.3(\rho_{800} - \rho_{550})]}{\sqrt{(2\,\rho_{800} + 1)^2 - 6\,\rho_{800} - 5\sqrt{\rho_{670}} - 0.5}}$	[31]
29	7	Modified Red Edge NDVI	$MRENDVI = \frac{\rho_{750} - \rho_{705}}{\rho_{750} + \rho_{705} - 2\rho_{445}}$	[55]
20	5	Modified Triangular Vegetation Index	$MTVI = 1.44\,(\rho_{800} - \rho_{550}) - 3\,(\rho_{670} - \rho_{550})$	[31]
4	33	Non-Linear Index	$NLI = \frac{NIR^2 - Red}{NIR^2 + Red}$	[56]
24	2	Normalized Difference Mud Index	$NDMI = \frac{\rho_{795} - \rho_{990}}{\rho_{795} + \rho_{990}}$	[57]
13	28	Normalized Difference Snow Index	$NDSI = \frac{Green - NIR}{Green + NIR}$	[58]
10	16	Normalized Difference Vegetation Index	$NDVI = \frac{NIR - Red}{NIR + Red}$	[17]
36	25	Photochemical Reflectance Index	$PRI = \frac{\rho_{531} - \rho_{570}}{\rho_{531} + \rho_{570}}$	[59,60]
27	12	Plant Senescence Reflectance Index	$PSRI = \frac{\rho_{680} - \rho_{500}}{\rho_{750}}$	[61]
7	13	Red Edge NDVI	$RENDVI = \frac{\rho_{750} - \rho_{705}}{\rho_{750} + \rho_{705}}$	[62,63]
15	18	Renormalized Difference Vegetation Index	$RDVI = \frac{NIR - Red}{\sqrt{NIR + Red}}$	[64]
3	22	Simple Ratio	$SR = \frac{NIR}{Red}$	[33]
8	17	Soil Adjusted Vegetation Index	$SAVI = \frac{1.5(NIR - Red)}{NIR + Red + 0.5}$	[48]
33	36	Structure Insensitive Pigment Index	$SIPI = \frac{\rho_{800} - \rho_{445}}{\rho_{800} - \rho_{680}}$	[65]
34	27	Sum Green Index	$SGI = \frac{\mu(\rho_{500}, \ldots, \rho_{600})}{nBands(\rho_{500}, \ldots, \rho_{600})}$	[66]
32	1	Transformed CARI	$TCARI = 3[(\rho_{700} - \rho_{670}) - 0.2(\rho_{700} - \rho_{550})\frac{\rho_{700}}{\rho_{670}}]$	[31]
6	11	Transformed Vegetation Index	$TrVI = \sqrt{0.5 + \frac{NIR - Red}{NIR + Red}}$	[47]
21	4	Triangular Vegetation Index	$TVI = 0.5\,[120(\rho_{750} - \rho_{550}) - 200(\rho_{670} - \rho_{550})]$	[67]
23	10	Visible Atmospherically Resistant Index	$VARI = \frac{Green - Red}{Green + Red - Blue}$	[68]
2	35	Vogelmann Red Edge Index 1	$VRE1 = \frac{\rho_{740}}{\rho_{720}}$	[34]

Cerra et al., 2018

Detection of “marks”

Mutual Information

$$I(X,Y) = \sum_{x,y} p(x,y) \log \frac{p(x,y)}{p(x)p(y)}$$

Here $p(x)$ and $p(y)$ are the probability distributions of X and Y, while $p(x,y)$ is the joint probability of X and Y. The mutual information is positively defined, with a value $I(X,Y) = 0$

Selinunte

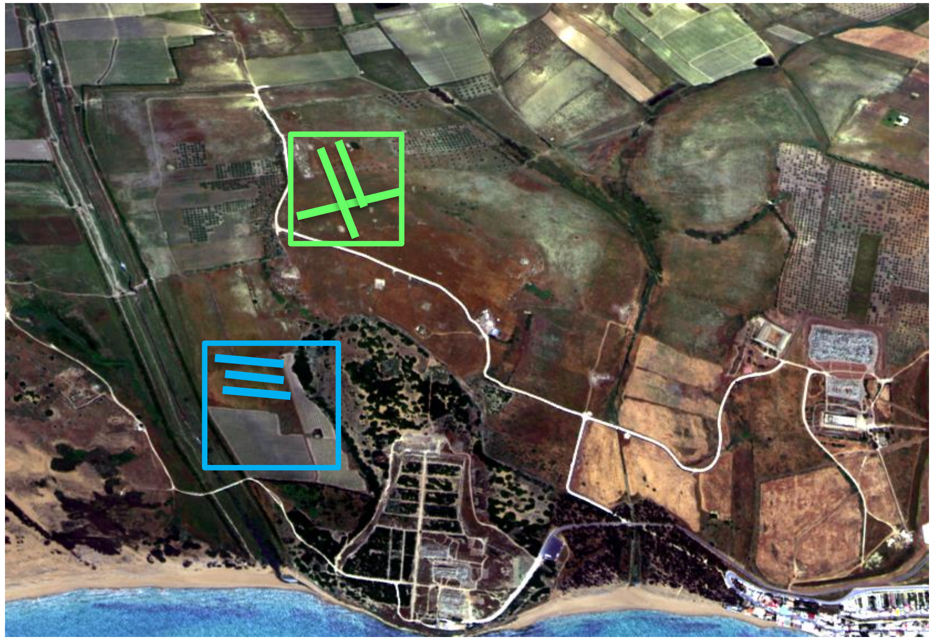

Cerra et al., 2018

The first parameter, the *Detection Index* (D.I.), provides a quantitative measure of photo-interpretation analysis done on the images. D.I. is expressed by the following relation:

$$\text{D.I.} = \frac{Npixel_{\text{archa}}}{Npixel_{t-\text{archa}}} \times 100 \qquad (1)$$

where, for a given area, $Npixel_{\text{archa}}$ is the number of pixels belonging to the archaeological marks in the interpreted image, while $Npixel_{\text{t-archa}}$ corresponds to the total number of pixels recognized as archaeological marks in the whole set of analysed images.

In contrast, the *Separation Index* (S.I.), gives an indication of the tonal difference between archaeological marks and background. The index is expressed as follows:

$$\text{S.I.} = \left(1 - \frac{\int D_{\text{archa}} D_{\text{bck}} \mathrm{d}x}{\sqrt{\int D^2_{\text{archa}} \mathrm{d}x \int D^2_{\text{bck}} dx}}\right) \times 100 \qquad (2)$$

where D_{archa} represents the frequency distribution of the digital values of the pixels belonging to the archaeological marks ($Npixel_{\text{archa}}$), while D_{bck} represents the frequency distribution of the pixels selected as background. S.I. is, therefore, an indicator of the overlapping area of the two frequency distributions D_{archa} and D_{bck}.

Cavalli et al., 2007

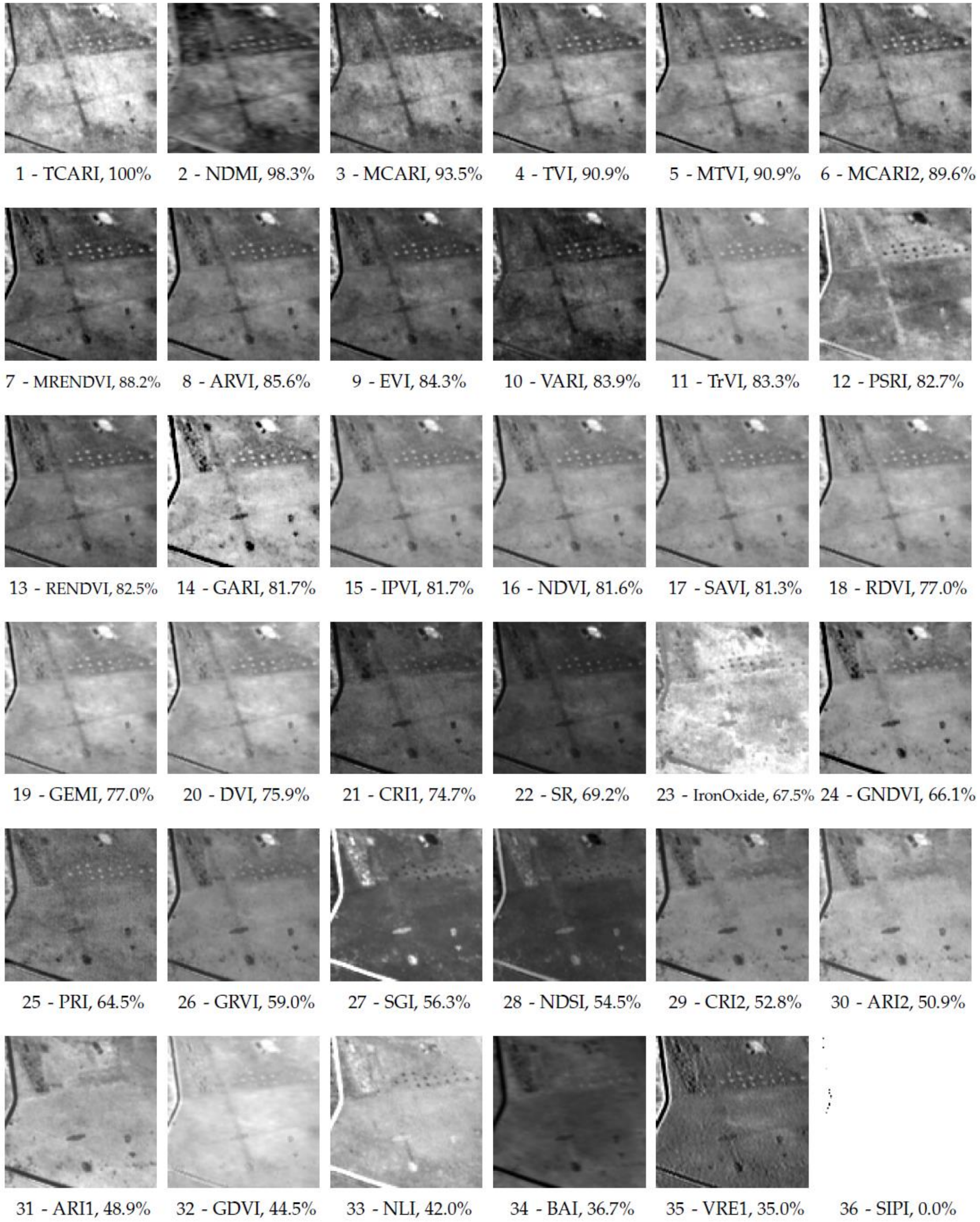

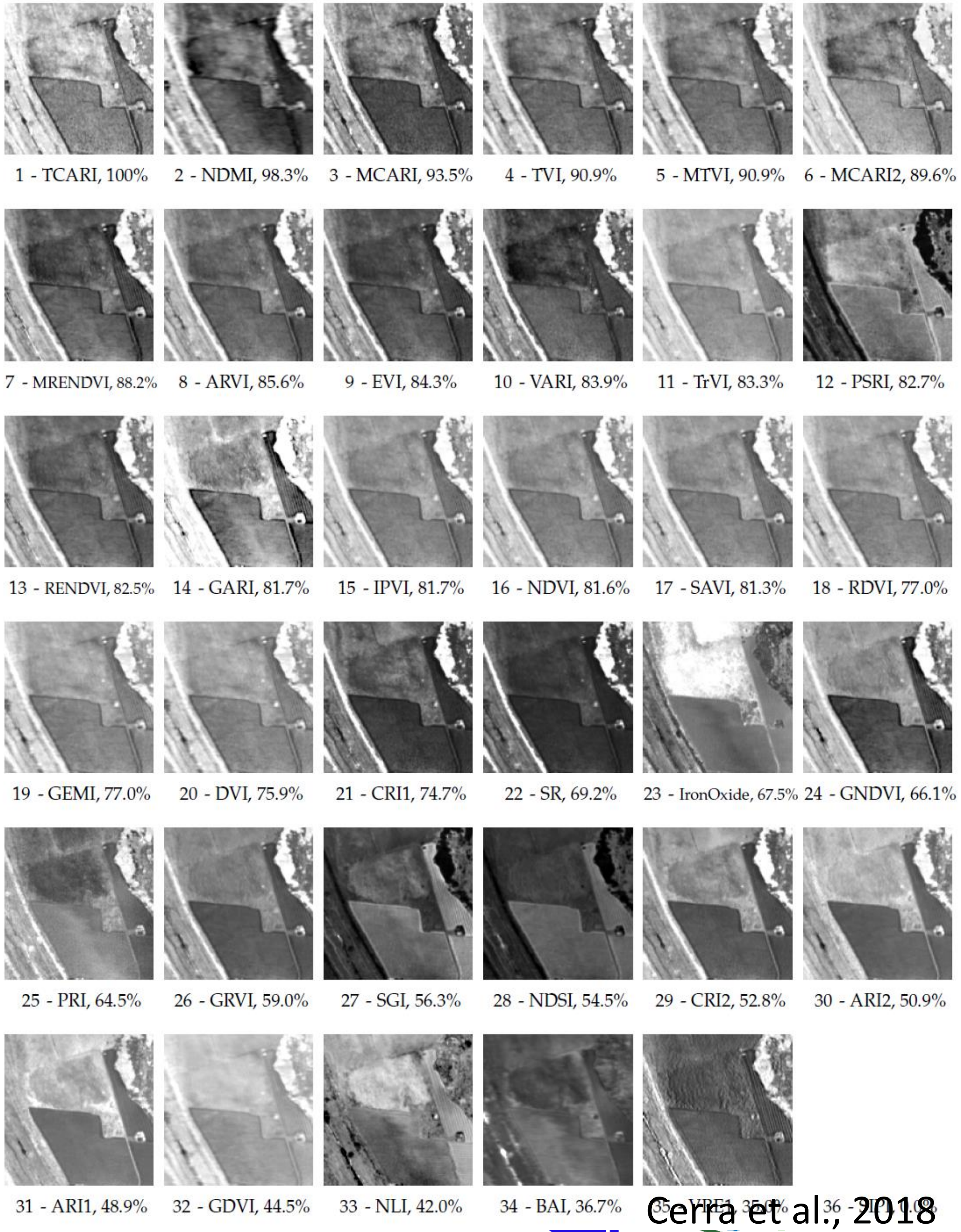

Cerra et al., 2018

Detection of “marks”

Selinunte

Cavalli et al., 2007

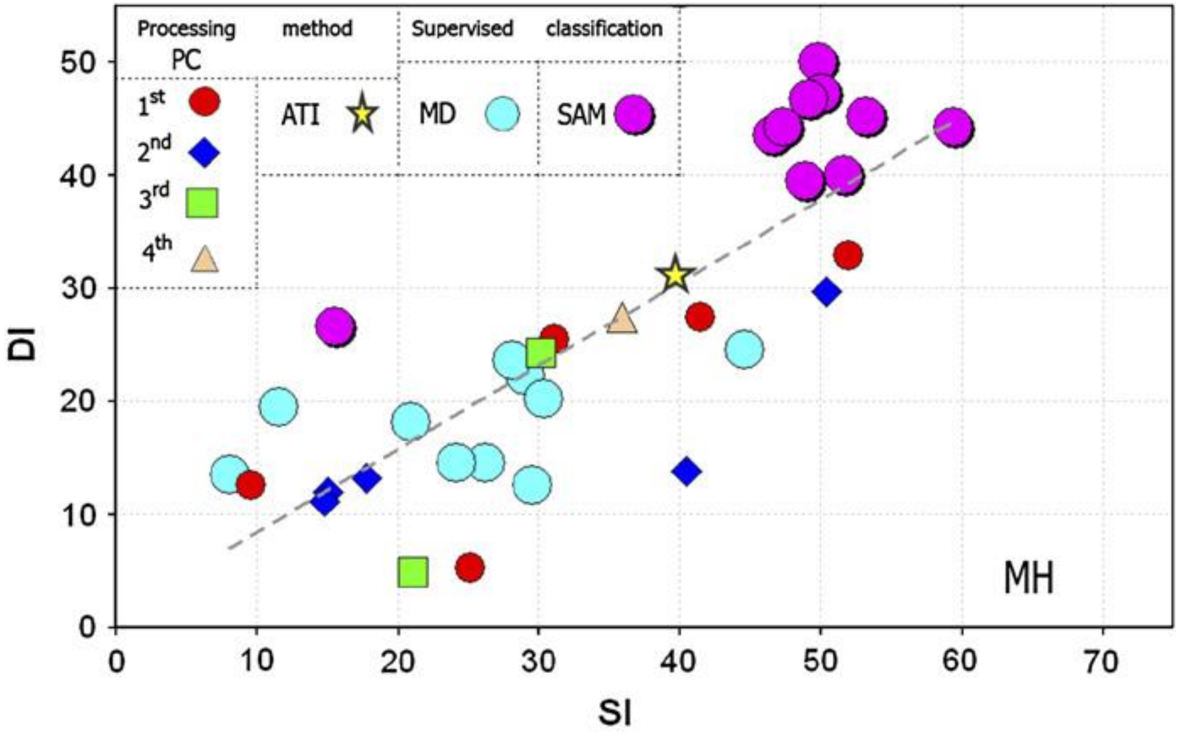

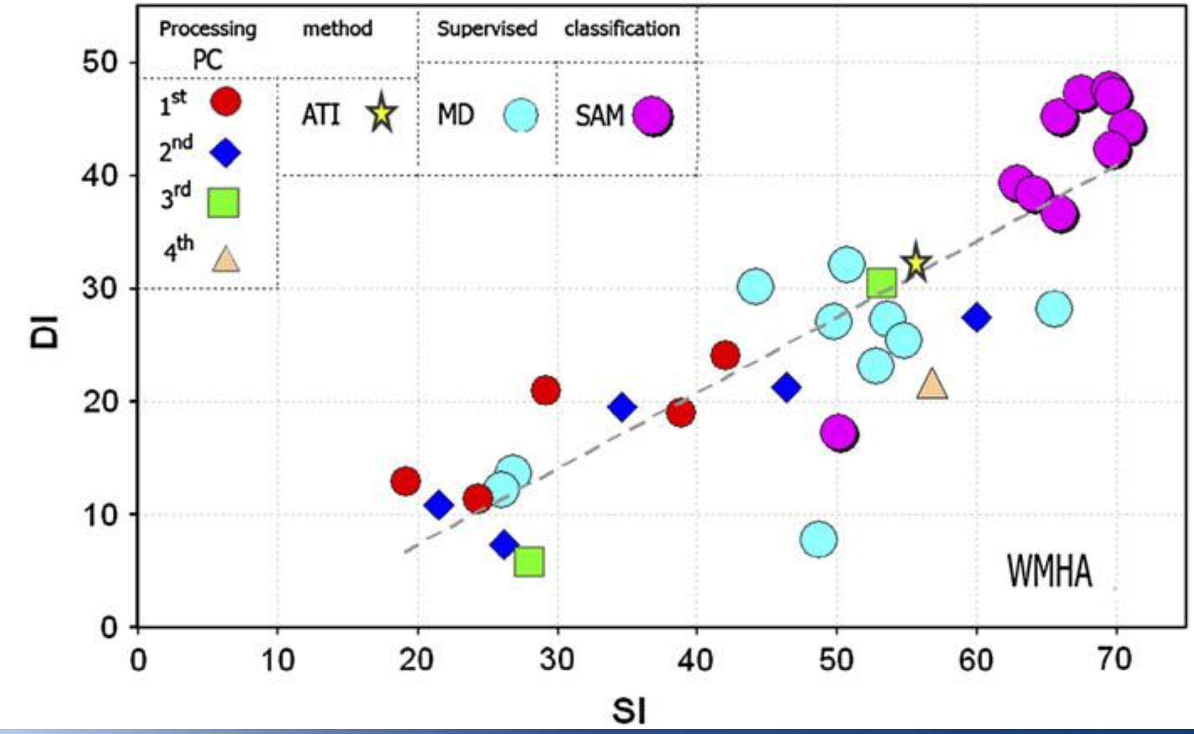

Detection of “marks”

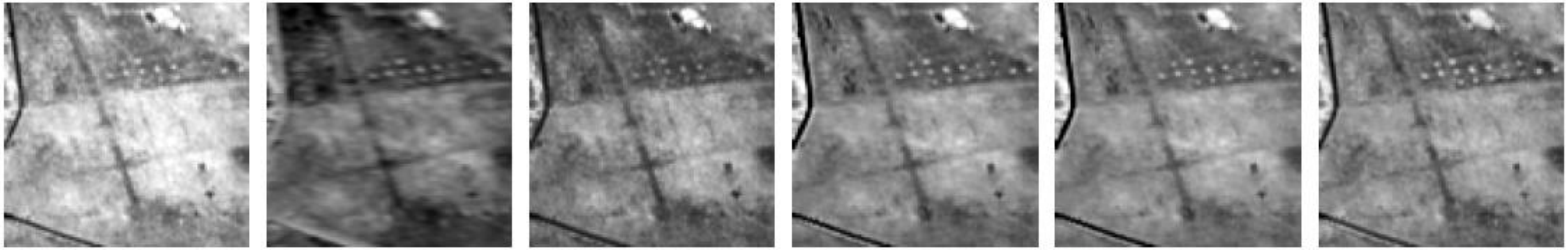

1 - TCARI, 100% | 2 - NDMI, 98.3% | 3 - MCARI, 93.5% | 4 - TVI, 90.9% | 5 - MTVI, 90.9% | 6 - MCARI2, 89.6%

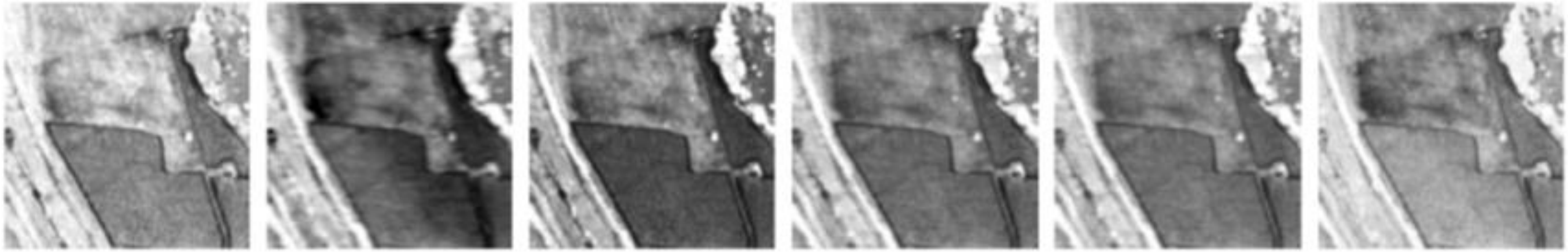

1 - TCARI, 100% | 2 - NDMI, 98.3% | 3 - MCARI, 93.5% | 4 - TVI, 90.9% | 5 - MTVI, 90.9% | 6 - MCARI2, 89.6%

Detection of “marks”

Cavalli et al., 2007

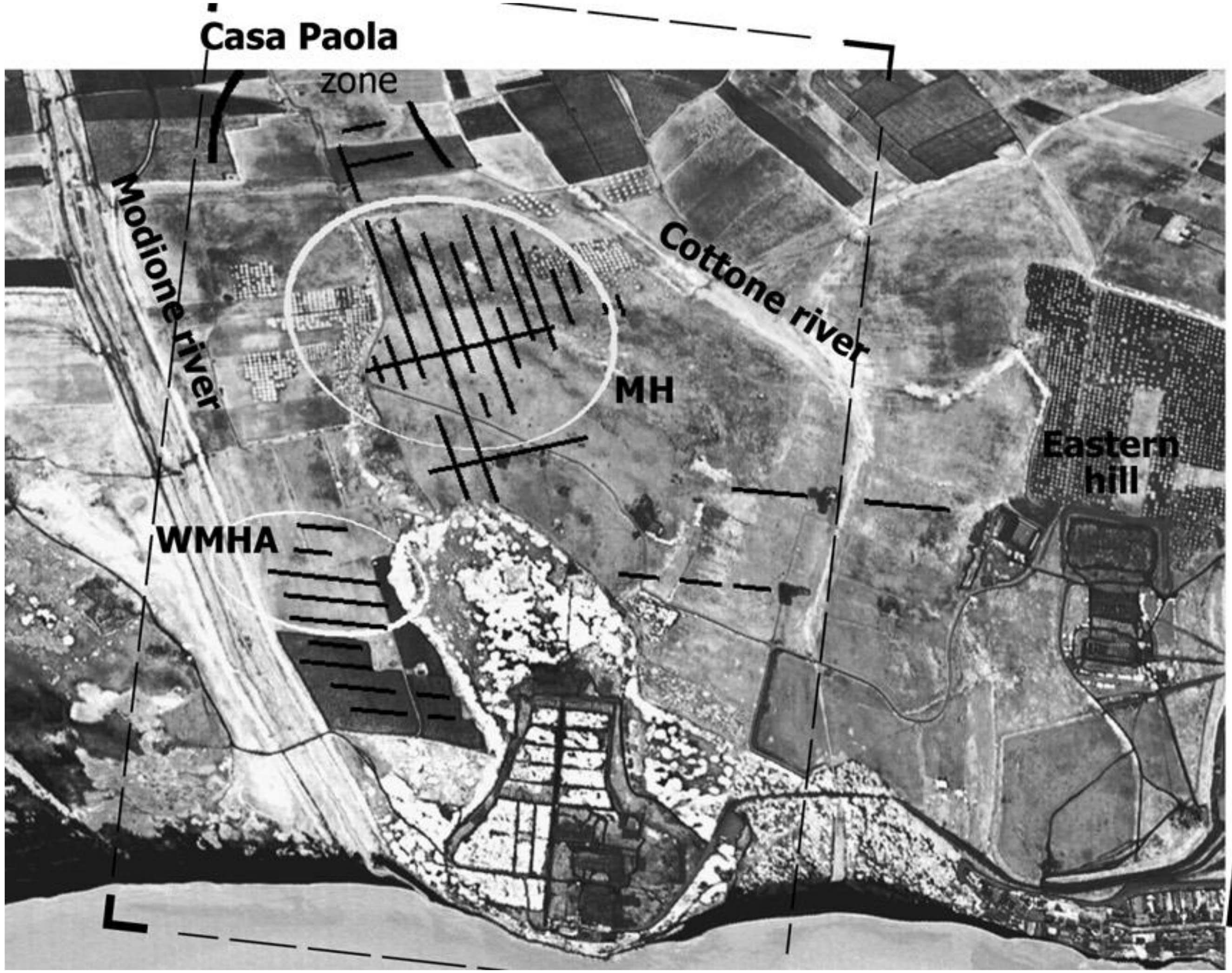

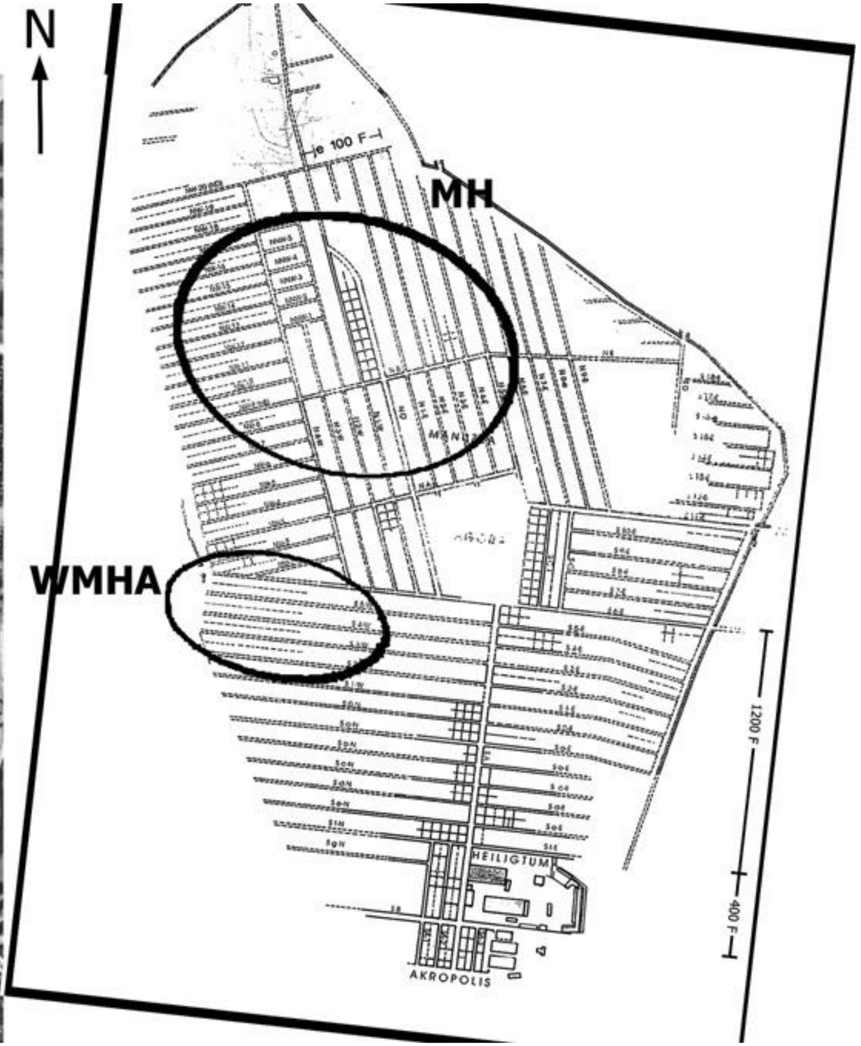

The left picture shows the ensemble of the archaeological anomalies highlighted by all by-products of M.I.V.I.S. data; the right picture shows the street network highlighted by the geophysical surveys (Mertens, 2003)

References

- Bassani, C., Cavalli, R. M., Goffredo, R., Palombo, A., Pascucci, S., & Pignatti, S. (2009). Specific spectral bands for different land cover contexts to improve the efficiency of remote sensing archaeological prospection: The Arpi case study. *Journal of Cultural Heritage*, *10*, e41-e48.
- Cavalli, R. M., Colosi, F., Palombo, A., Pignatti, S., & Poscolieri, M. (2007). Remote hyperspectral imagery as a support to archaeological prospection. *Journal of Cultural Heritage*, *8*(3), 272-283.
- Cavalli, R. M., Licciardi, G. A., & Chanussot, J. (2012). Detection of anomalies produced by buried archaeological structures using nonlinear principal component analysis applied to airborne hyperspectral image. *IEEE Journal of Selected Topics in Applied Earth Observations and Remote Sensing*, *6*(2), 659-669.
- Cerra, D., Agapiou, A., Cavalli, R. M., & Sarris, A. (2018). An objective assessment of hyperspectral indicators for the detection of buried archaeological relics. *Remote Sensing*, *10*(4), 500.
- D. Mertens, I. Selinus, Die Stadt und ihre Mauern, Verlag Philipp von Zaberm, Mainz am Rein, Germany, 2003.
- Pascucci, S., Cavalli, R. M., Palombo, A., & Pignatti, S. (2010). Suitability of CASI and ATM airborne remote sensing data for archaeological subsurface structure detection under different land cover: the Arpi case study (Italy). Journal of Geophysics and Engineering, 7(2), 183-189.

Conclusions

In the current technological and scientific context, to evaluate and compare the capabilities of different remote sensing data and to compare the results of different methods allows us to:

- identify the most suitable images and methodologies;
- and/or decide on the integration with other images and/or data;
- and/or opt for the complementary use of different methodologies.